Cell Reports
Methods

Article

CUBIC-Cloud provides an integrative computational framework toward community-driven whole-mouse-brain mapping

Graphical abstract

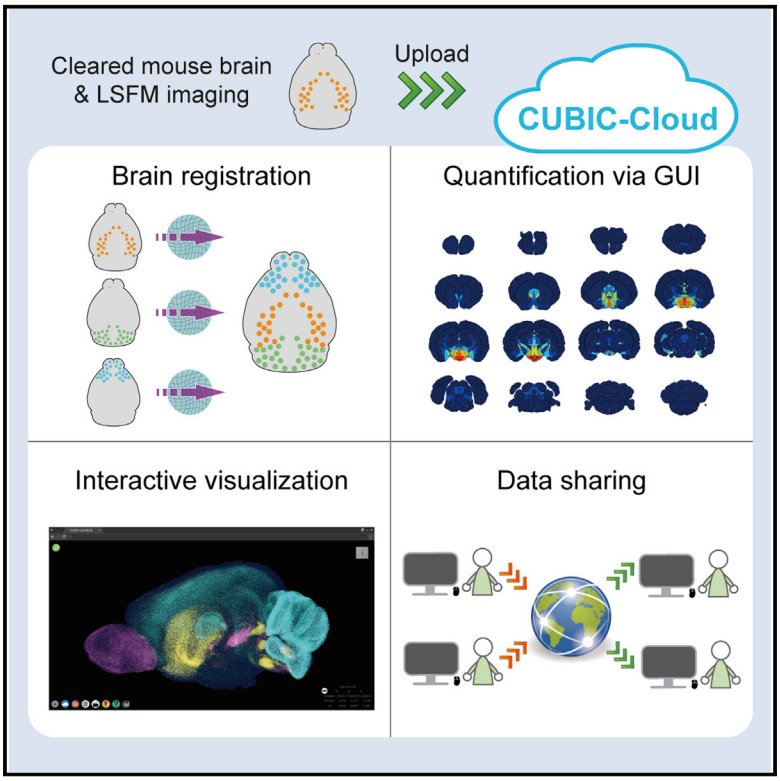

Authors

Tomoyuki Mano, Ken Murata, Kazuhiro Kon, ..., Etsuo A. Susaki, Kazushige Touhara, Hiroki R. Ueda

Correspondence

uedah-tky@umin.ac.jp

In brief

CUBIC-Cloud is a cloud-native image analysis platform for whole-mouse-brain analysis, offering analysis, visualization, and sharing of the 3D images through an interactive web browser interface. Mano et al. demonstrate the applications of CUBIC-Cloud in (1) cell type mapping, (2) IEG profiling, and (3) connectivity mapping by using rabies virus.

Highlights

- CUBIC-Cloud is a cloud-native software for whole-mouse-brain analysis
- CUBIC-Cloud allows scalable analysis of dozens of whole mouse brains
- Whole-brain, cell type, and IEG mapping by using antibody labeling was demonstrated
- Connectivity of Kiss1 neurons in ARH was investigated by using rabies virus

Mano et al., 2021, Cell Reports Methods *1*, 100038
June 21, 2021
https://doi.org/10.1016/j.crmeth.2021.100038

CellPress

Cell Reports Methods

CellPress
OPEN ACCESS

Article

CUBIC-Cloud provides an integrative computational framework toward community-driven whole-mouse-brain mapping

Tomoyuki Mano,[1,2,6] Ken Murata,[3] Kazuhiro Kon,[4] Chika Shimizu,[2] Hiroaki Ono,[4,7] Shoi Shi,[2,4] Rikuhiro G. Yamada,[2] Kazunari Miyamichi,[3,8] Etsuo A. Susaki,[2,4,9] Kazushige Touhara,[3,5] and Hiroki R. Ueda[1,2,4,10,*]

[1]Department of Information Physics and Computing, Graduate School of Information Science and Technology, The University of Tokyo, Bunkyo-ku, Tokyo 113-0033, Japan
[2]Laboratory for Synthetic Biology, RIKEN Center for Biosystems Dynamics Research, Suita, Osaka 565-5241, Japan
[3]Department of Applied Biological Chemistry, Graduate School of Agricultural and Life Sciences, The University of Tokyo, Bunkyo-ku, Tokyo 113-8657, Japan
[4]Department of Systems Pharmacology, Graduate School of Medicine, The University of Tokyo, Bunkyo-ku, Tokyo 113-0033, Japan
[5]International Research Center for Neurointelligence (WPI-IRCN), UTIAS, The University of Tokyo, Bunkyo-ku, Tokyo 113-0033, Japan
[6]Present address: Computational Neuroethology Unit, Okinawa Institute of Science and Technology, Onna, Okinawa 904-0495, Japan
[7]Present address: Laboratory of Retinal Regeneration, RIKEN Center for Biosystems Dynamics Research, Kobe, Hyogo 650-0047, Japan
[8]Present address: Laboratory for Comparative Connectomics, RIKEN Center for Biosystems Dynamics Research, Kobe, Hyogo 650-0047, Japan
[9]Present address: Department of Biochemistry and Systems Biomedicine, Graduate School of Medicine, Juntendo University, Bunkyo-ku, Tokyo 113-8421, Japan
[10]Lead contact
*Correspondence: uedah-tky@umin.ac.jp
https://doi.org/10.1016/j.crmeth.2021.100038

MOTIVATION With the advancement of tissue clearing technology and 3D imaging methods, researchers are able to rapidly obtain whole mouse brain images at single-cell resolution. Because of the massive size of the resulting images, however, a high-throughput yet highly accessible image analysis method is needed to scale up 3D profiling of the brain. In addition, effective data sharing is critical to maximize the potential value of the 3D image dataset. Here, we address these challenges by designing an end-to-end image analysis platform embracing the latest cloud technology, named CUBIC-Cloud.

SUMMARY

Recent advancements in tissue clearing technologies have offered unparalleled opportunities for researchers to explore the whole mouse brain at cellular resolution. With the expansion of this experimental technique, however, a scalable and easy-to-use computational tool is in demand to effectively analyze and integrate whole-brain mapping datasets. To that end, here we present CUBIC-Cloud, a cloud-based framework to quantify, visualize, and integrate mouse brain data. CUBIC-Cloud is a fully automated system where users can upload their whole-brain data, run analyses, and publish the results. We demonstrate the generality of CUBIC-Cloud by a variety of applications. First, we investigated the brain-wide distribution of five cell types. Second, we quantified Aβ plaque deposition in Alzheimer's disease model mouse brains. Third, we reconstructed a neuronal activity profile under LPS-induced inflammation by c-Fos immunostaining. Last, we show brain-wide connectivity mapping by pseudotyped rabies virus. Together, CUBIC-Cloud provides an integrative platform to advance scalable and collaborative whole-brain mapping.

INTRODUCTION

Massive and collective observation of complex systems (often referred to as omics approaches) is the driving force of modern biology. It would also be true for studying highly evolved mammalian brains, in which a complex system of intricately connected cells gives rise to intelligent behaviors. In particular, comprehensive approaches to identifying the properties of every single cell *in situ* within this complex system would be pivotal. Recent advancements in tissue clearing technology have brought new breakthroughs in this landscape (Dodt et al., 2007; Hama et al., 2011; Ertürk et al., 2012; Ke et al., 2013;

Chung et al., 2013; Yang et al., 2014; Susaki et al., 2014; Tainaka et al., 2014; Belle et al., 2017). Combined with light-sheet fluorescence microscopy (LSFM) (Power and Huisken, 2017) and genetic, viral, and immunohistochemical labeling techniques, tissue clearing now enables high-speed volumetric imaging of mammalian (most prominently mouse) brains at cellular resolution (Susaki et al., 2014; Renier et al., 2014; Murray et al., 2015; Hama et al., 2015; Chan et al., 2017; Kubota et al., 2017; Cai et al., 2019; Kirst et al., 2020). Built on top of these technological advancements, we recently reported the construction of CUBIC-Atlas (Murakami et al., 2018), a 3D mouse brain atlas with single-cell resolution, where all of the cells in the brain (amounting to approximately 0.1 billion) were digitally analyzed and recorded.

These scientific advancements encourage us to conceive a future where whole-brain mapping projects, which conventionally required institution-scale resources and efforts, can be carried out by individual laboratories, or even by a single researcher (Tainaka et al., 2016; Susaki and Ueda, 2016; Mano et al., 2018; Gradinaru et al., 2018). In this regard, the current technological stage can be thought of as parallel to the dawn of genome sequencing technology in the early 2000s. In genome science, the importance of the data repository cannot be overstated. The emergence of the database to browse and search genomes (such as the UCSC Genome Browser) (Karolchik et al., 2009) played a critical role in integrating data collected in numerous sites across the globe. Such distributed collaboration prompted a rapidly growing coverage of various organisms and individuals, pioneering the data-driven discoveries of gene functions and new therapeutics. In neuroscience, several large-scale mouse brain datasets have been constructed, such as the Allen Mouse Brain Atlas (Wang et al., 2020) and Brain Architecture Project (Kim et al., 2017), primarily by using serial sectioning tomography methods. However, a common platform embracing the tissue-clearing and rapid brain-scanning techniques that offers the opportunity for the community to submit and share new data has yet to appear. On the basis of these considerations, we suggest that it is now possible to construct a community-supported mouse brain data repository, borrowing collaborative ideas from the genome sciences.

By referring to the previous image analysis pipelines for tissue clearing samples (Frasconi et al., 2014; Susaki et al., 2015; Renier et al., 2016; Cai et al., 2019; Fürth et al., 2018), we postulated that the following elements should be considered in composing a framework for whole mouse brain mapping. First, a reference brain (equivalent to the template sequence), to which all brain data are aligned, is necessary. We think that CUBIC-Atlas would play a central role in addressing this challenge. Second, the framework should be constructed around the research community, which allows researchers to submit the data, as well as browsing and searching the brains in the previous studies. Third, because of the complexity and the large size of the whole-brain datasets, the framework should be equipped with a toolkit to visualize and quantify the data to assist intuitive understanding. Fourth, these software tools should offer superior accessibility and usability to the end users, without requiring specialized expertise in programming or powerful computer resources.

In this paper, we present a computational framework for single-cell-resolution whole mouse brain analysis, named CUBIC-Cloud. We built CUBIC-Cloud on top of the latest cloud computing technologies. After identifying single cells from a 3D image stack, users can upload the structure image and detected cell list to the CUBIC-Cloud server. The CUBIC-Cloud server automatically aligns individual brains with the CUBIC-Atlas and constructs the user's own mouse brain database. CUBIC-Cloud also offers graphical user interface (GUI) tools to perform various kinds of quantification tasks. Uploaded brains can be interactively visualized by using the 3D brain viewer. The scientific results obtained thereby can be easily published in CUBIC-Cloud's public repository, to allow other researchers to view the data. CUBIC-Cloud is hosted at https://cubic-cloud.com.

After describing the software architecture, we extensively demonstrate the capability and generality of the CUBIC-Cloud framework by analyzing over 50 whole mouse brains, covering four important application domains: (1) investigating the distribution of targeted cell types ("cell type mapping"), (2) quantifying the pathological state by disease markers, (3) reconstructing the neuronal activity profile by imaging the expression of c-Fos ("activity mapping"), and (4) deciphering brain-wide connectivity by using rabies virus (RV) tracers ("circuit mapping"). With these applications, we established a general framework to effectively integrate whole-brain mapping experiments, offering new opportunities for data-driven discoveries in neuroscience.

RESULTS

CUBIC-Cloud whole-brain analysis framework

To design a unified workflow for whole mouse brain analysis, we constructed CUBIC-Cloud on top of our previously published tissue clearing protocols and brain mapping strategies (Susaki et al., 2014; Murakami et al., 2018; Tainaka et al., 2018). The workflow of whole-brain analysis using CUBIC-Cloud is illustrated in Figure 1. Briefly, the workflow divides into (1) tissue clearing and image collection, (2) single-cell detection, and (3) uploading the data to CUBIC-Cloud, where brain registration, brain-wide quantification, and visualization are performed.

In this study, mouse brains were cleared by CUBIC-L and CUBIC-R+ reagents (Tainaka et al., 2018) (step 1 in Figure 1). In addition, nuclear counterstaining (for brain registration) and, optionally, immunostaining were applied by following the CUBIC-HV protocol (Susaki et al., 2020) (STAR Methods). In most experiments, cleared brains were imaged using macro-zoom LSFM with 6.5 μm isotropic XYZ voxel size (step 2 in Figure 1 and STAR Methods). The transparency of the cleared brain was quantitatively evaluated by imaging fluorescent beads embedded in the tissue, validating homogeneous image quality throughout all brain regions (Figure S2 and STAR Methods).

After we obtained the 3D image stack, we detected labeled cells by using ilastik software (Sommer et al., 2011; Berg et al., 2019) (step 3 in Figure 1). ilastik uses supervised machine learning (random forest algorithm) to classify pixels into multiple classes (such as cells and backgrounds), which performed robustly well even when cells from different brain regions presented diverse brightness and morphology. We created a Python script, which wrapped ilastik to automate the workflow

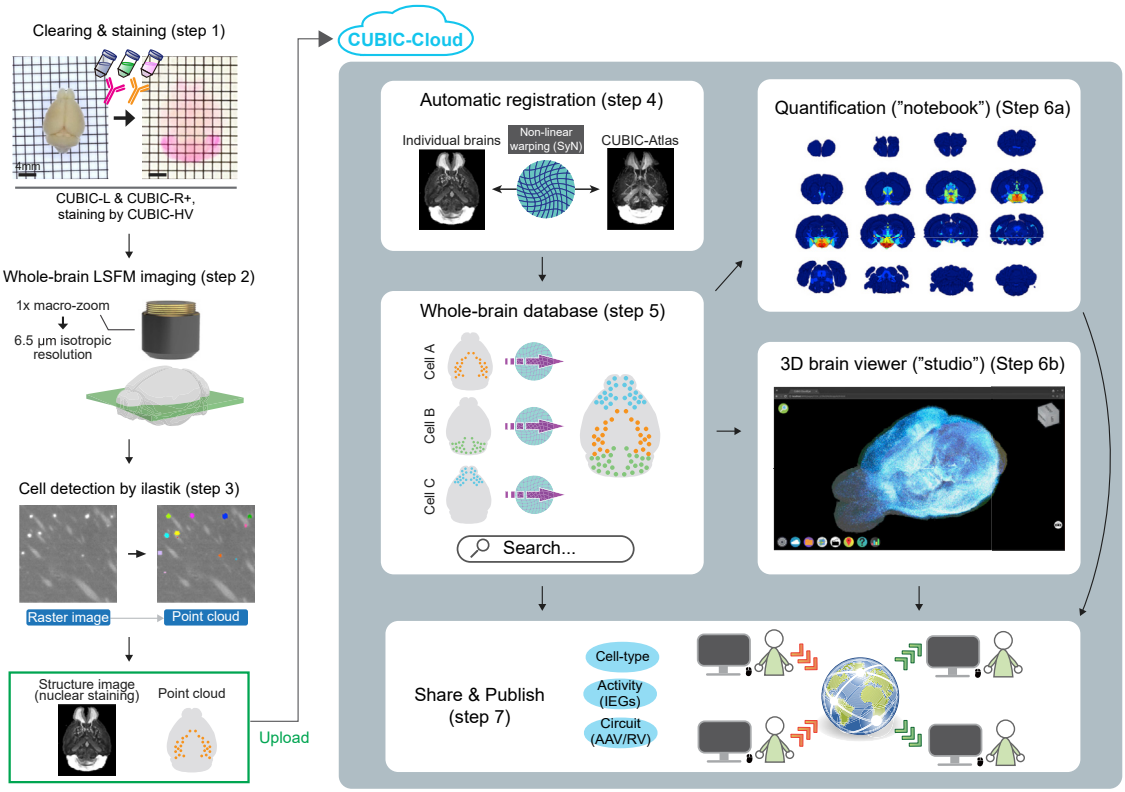

Figure 1. CUBIC-Cloud: A cloud-based computational framework for whole mouse brain analysis

Overview of the whole-brain analysis pipeline by CUBIC-Cloud. In this study, mouse brains were cleared by CUBIC-L and CUBIC-R+ reagents and 3D stained by the CUBIC-HV protocol. Cleared brains were imaged by using macro-zoom LSFM. From the obtained image stacks, single cells were isolated by using ilastik software, converting the raw raster image into an ensemble of discrete cells (i.e., point cloud). Users then upload the point-cloud cells and structure image to CUBIC-Cloud. In the cloud, brain registration is automatically performed to align individual brains with the reference brain. Thereby, the user's own brain database is constructed. Then, the user can perform various kinds of brain-wide quantification using "notebook." CUBIC-Cloud also offers an interactive 3D whole-brain viewer ("studio"). Last, CUBIC-Cloud lets users share and publish their point-cloud whole-brain data, as well as notebooks and studios, to allow broad access to researchers. Abbreviation are as follows: AAV/RV, adeno-associated virus/rabies virus; IEGs, immediate-early genes.

and add some custom analysis routines (STAR Methods). The accuracy of cell counting is described in the corresponding sections. By this cell counting procedure, raw raster images were converted into a discrete ensemble of cellular points, or a point cloud, where positions, volumes, and fluorescence intensities of all labeled cells in the brain were recorded. Of note, users can opt to use their own cell detection routine, as long as the output follows the format required by CUBIC-Cloud.

After cell detection, the rest of the analyses were carried out by CUBIC-Cloud (Video S1). Users can go to the CUBIC-Cloud website (https://cubic-cloud.com) and upload their cellular point cloud and corresponding structure image (nuclear staining channel) to the server. CUBIC-Cloud is deployed on Amazon Web Service (AWS by) using the so-called serverless architecture. Serverless architecture allows the cloud to dynamically scale its capacity based on the computational load, enabling the cloud to handle a practically unlimited number of tasks in parallel while minimizing the idling time. The detailed implementation is described in the STAR Methods (also see Figure S1). Once the brain data are uploaded to the CUBIC-Cloud server, they are automatically sent to the preprocessing task queue, which is powered by ECS and EC2 on AWS. The preprocessing task first performs brain registration to align the submitted brain with the CUBIC-Atlas (step 4 in Figure 1). CUBIC-Cloud uses the symmetric diffeomorphic image registration (SyN) algorithm implemented in the ANTs library (Avants et al., 2008). Using the nuclear staining channel, SyN iteratively optimizes the warp field to maximize the normalized cross-correlation, which measures the similarity between two images (Figure S3I and S3J and STAR Methods). After registration, cell coordinates are transformed to the CUBIC-Atlas space, and all cells are given anatomical region IDs (following the Allen Brain Atlas CCF v.3) (Wang et al., 2020).

By repeating the above procedures, users can construct their own brain database in CUBIC-Cloud. As the database grows, users can search brains using tags attached to them, such as cell labels and project names, along with other metadata. To perform quantitative analysis of the brains in the database, CUBIC-Cloud offers a "notebook," a feature that allows users to create various kinds of graphs with a GUI (step 6a in Figure 1). To give some concrete examples, many of the figure items presented in this paper were created by CUBIC-Cloud's notebook.

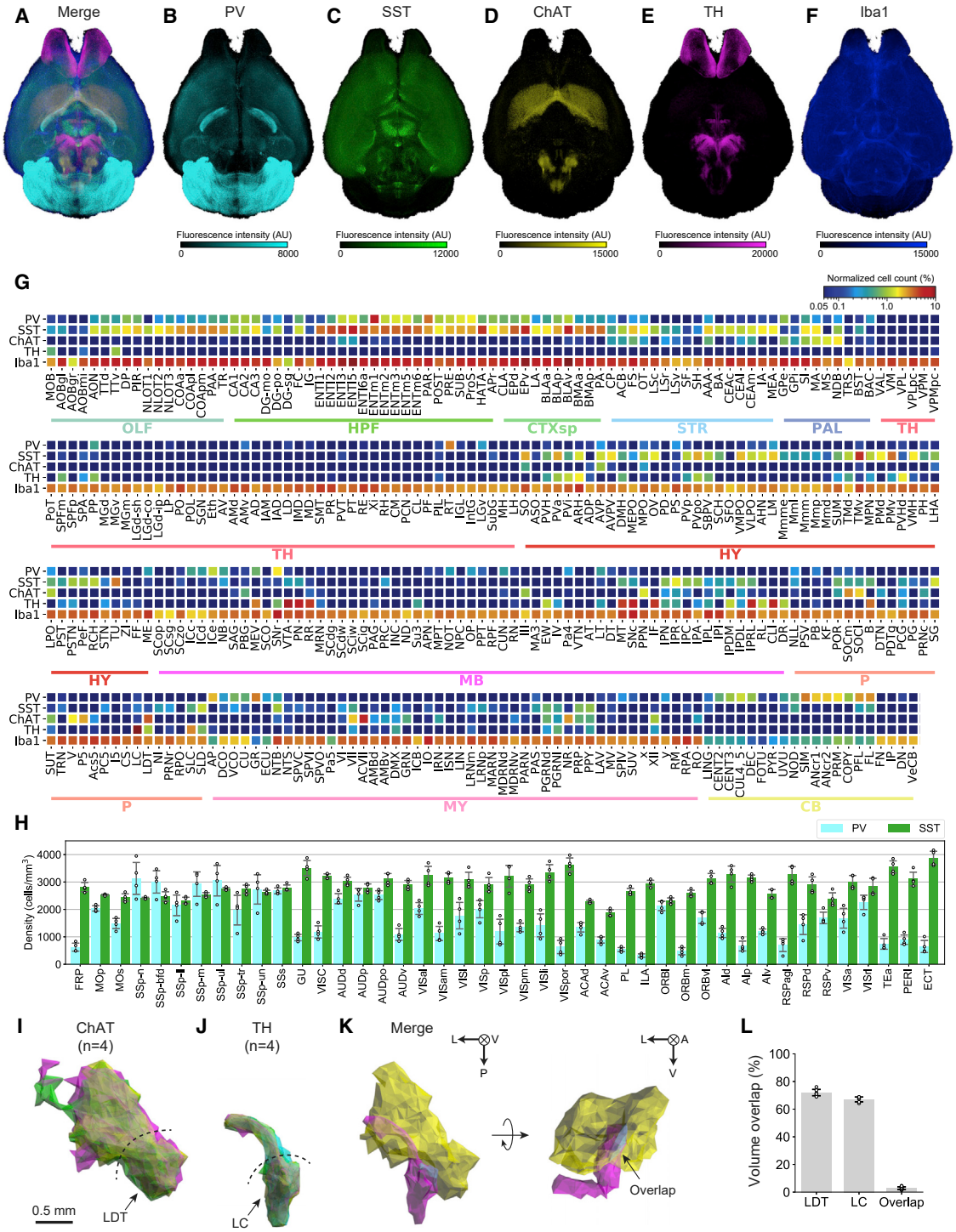

Figure 2. Whole-brain analysis of PV-, SST-, ChAT-, and TH-expressing cells

Whole-brain distribution of PV-, SST-, ChAT-, TH-, and Iba1-expressing cells was investigated by applying 3D immunostaining and by using the CUBIC-Cloud analysis framework.

(A–F) Whole-brain views of labeled cells. Each point (i.e., single cell) was assigned a pseudo-color on the basis of its fluorescence intensity. (A) Merge, (B) PV, (C) SST, (D) ChAT, (E) TH, (F) Iba1.

(G) Relative population heatmap of all brain regions outside the isocortex. The number of each cell type was normalized by the total number of cells in each region, derived from CUBIC-Atlas (n = 4 for PV, SST, ChAT, and TH; n = 7 for Iba1).

(H) Density of PV- and SST-expressing cells in the isocortex. Data are shown as the mean ± SD (n = 4).

(legend continued on next page)

CUBIC-Cloud also offers an interactive 3D brain viewer, a feature called ''studio'' (step 6b in Figure 1). Here, brain data are visualized in point-cloud format, where the whole brain is rendered as an ensemble of discrete cellular points, each carrying biological attributes such as protein expression levels. Point-cloud format is more efficient for delivering data to the remote clients than sending raw raster data, while carrying the essential biological information. The viewer runs on standard web browsers, and the point clouds are adaptively queried from the server upon the viewer's camera movement, enabling one to interact with millions of cells in real time.

The last essential component of CUBIC-Cloud is sharing and publishing. Users can share their whole-brain data with specific users, such as research collaborators, and grant access to the data. Users can opt to publish their data in the CUBIC-Cloud's public repository. Once published, any users can view the brain. The share and publish capability is also supported for the notebooks and studios. Therefore, users can transparently show their analysis results to the research community. To demonstrate this concept, all of the brain data investigated in this study are deposited on the CUBIC-Cloud public repository, as well as the notebooks and studios that performed the analysis. Together, CUBIC-Cloud offers a cloud-native and integrative software solution for whole mouse brain mapping.

To maintain the cloud service, CUBIC-Cloud offers both free and paid subscription plans. With the free subscription, users can view the published data and try the analysis of several brains. By publishing the brain data in the public repository, users are offered a bonus token, which can be used to analyze other brains. To analyze more brains than the free plan limit, users need to sign up for the paid subscription. The subscription policies are subject to changes in the future and can be checked at the website (https://cubic-cloud.com/subscription_plans).

Whole-brain analysis of PV-, SST-, ChAT-, and TH-expressing cells

In the following, we use CUBIC-Cloud in several neuroscience applications to show the generality of the proposed framework. As the first application, we attempted to quantify the whole-brain distribution of distinct cellular subtypes that express the following markers: parvalbumin (PV), somatostatin (SST), choline acetyltransferase (ChAT), tyrosine hydroxylase (TH), and ionized calcium-binding adapter molecule 1 (Iba1). Whole-brain-scale analyses of PV-, SST-, and ChAT-expressing neurons were previously reported using a knock-in transgenic mouse line with Cre recombinase and fluorescent proteins (Kim et al., 2017; Zhang et al., 2017; Li et al., 2018). However, no such whole-brain-scale analyses have been done so far using immunostaining and tissue clearing. Immunostaining offers several orthogonal advantages over genetic approaches, such as the capability to assess the absolute expression amount, and thus is of significant value. Therefore, we used the CUBIC-HV protocol (Susaki et al., 2020) to label the whole adult brain tissue with PV, SST, ChAT, TH, and Iba1 antibodies (STAR Methods).

The obtained images contained strong and soma-localized signals as well as moderately bright fibrous structures. Here, we attempted to quantify the number of immunoreactive cell bodies, and thus, the ilastik classifier was trained to isolate cell soma and reject fiber-like signals. The accuracy of the cell detection was extensively evaluated (Figures S3C–S3G). Our cell detection demonstrated 75%–95% precision and 60%–85% sensitivity for the regions evaluated, which we concluded was accurate enough to perform quantitative analysis.

Whole-brain views of the investigated cell types are shown in Figures 2A–2F (rendered by CUBIC-Cloud's 3D viewer). Here, cells are pseudo-colored, reflecting the fluorescence intensity of the immunostaining. In our analysis, the total numbers of detected cells were $(6.1 \pm 0.7) \times 10^5$ (PV, n = 4), $(6.7 \pm 0.3) \times 10^5$ (SST, n = 4), $(6.5 \pm 0.2) \times 10^4$ (ChAT, n = 4), $(6.9 \pm 1.2) \times 10^4$ (TH, n = 4), and $(2.72 \pm 0.14) \times 10^6$ (Iba1, n = 4) (Tables S1 and S2). In this paper, mean ± SD is used unless otherwise specified. The relative ratio of each cell type in all brain regions except isocortex is shown in Figure 2G. Here, the ratio was calculated by dividing the detected cell count by the total number of cells reported in CUBIC-Atlas (Murakami et al., 2018). We will discuss the brain-wide distribution of these cell types in more detail in the STAR Methods.

Within the isocortex, PV neurons were most densely populated in somatosensory and auditory areas, whereas there were relatively sparse populations in medial frontal and lateral association areas (Figure 2H). Compared with PV, SST neurons were more homogeneously observed in the isocortex, consistent with the Cre-based study by Kim et al. (2017). Laminar density analysis revealed that there were almost no PV cells in layer 1, and that cell density reached its peak in layer 4 or 5 for both PV and SST (Figures S5A–S5D), successfully recapitulating the previous observations (Gonchar et al., 2007; Xu et al., 2010). There were sparse populations of ChAT neurons, whose ChAT expression levels were very low (Figures S5E and S5F). These ChAT neurons were most dense in layer 2/3 or 4, corroborating the previous observation (Gonchar et al., 2007). For TH neurons, no significant population above false-positive detection level was found in the isocortex. Iba1-expressing cells were ubiquitously observed in the isocortex, with similar density across layers.

In terms of the expression levels per cell, again, PV^+ neurons showed large variance across cortical areas. As shown in Figures S5I–S5N, some of the regions, like the primary somatosensory area, mouth domain (SSp-m), and primary visual area (VISp), had a long tail in the distribution of the expression level, meaning that there was a population of neurons expressing a high amount of PV. On the other hand, regions like the ILA and ectorhinal area (ECT) had a very short-tailed profile, meaning that most of the cells had a weak PV expression. In stark

(I) From the cluster of ChAT-expressing cells, the boundary surface including LDT was extracted (n = 4).
(J) From the cluster of TH-expressing cells, the boundary surface including LC was extracted (n = 4).
(K) Merge of the two boundary surfaces (color coding is as follows: yellow, ChAT; magenta, TH; cyan, overlapping region).
(L) The volume overlaps of the boundary surfaces. Data are shown as mean ± SD (n = 4). Brain region acronyms follow the ontology defined by the Allen Brain Atlas.

Table 1. Brain region acronyms used in this paper

Acronym	Full name
AAA	anterior amygdalar area
ACB	nucleus accumbens
ADP	anterodorsal preoptic nucleus
AHN	anterior hypothalamic nucleus
ARH	arcuate hypothalamic nucleus
AVP	anteroventral preoptic nucleus
BST	bed nuclei of the stria terminalis
CEA	central amygdalar nucleus
CLI	central linear nucleus raphe
DMH	dorsomedial nucleus of the hypothalamus
DMX	dorsal motor nucleus of the vagus nerve
DTN	dorsal tegmental nucleus
FL	flocculus
HATA	hippocampo-amygdalar transition area
IA	intercalated amygdalar nucleus
IC	inferior colliculus
ILA	infralimbic area
IO	inferior olivary complex
LC	locus coeruleus
LDT	laterodorsal tegmental nucleus
LH	lateral habenula
LRN	lateral reticular nucleus
LS	lateral septal nucleus
LSr	lateral septal nucleus, rostral (rostroventral) part
LPO	lateral preoptic area
MEA	medial amygdalar nucleus
MEPO	median preoptic nucleus
MH	medial habenula
MRN	midbrain reticular nucleus
MPN	medial preoptic nucleus
MPO	medial preoptic area
NLL	nucleus of the lateral lemniscus
NOD	nodulus (X)
NTB	nucleus of the trapezoid body
NTS	nucleus of the solitary tract
PAG	periaqueductal gray
PB	parabrachial nucleus
PH	posterior hypothalamic nucleus
PP	peripeduncular nucleus
PVH	paraventricular hypothalamic nucleus
PVa	periventricular hypothalamic nucleus, anterior part
PVi	periventricular hypothalamic nucleus, intermediate part
PVp	periventricular hypothalamic nucleus, posterior part
PVpo	periventricular hypothalamic nucleus, preoptic part
PVT	paraventricular nucleus of the thalamus
RAmb	midbrain raphe nuclei
RL	rostral linear nucleus raphe
RR	midbrain reticular nucleus, retrorubral area
RT	reticular nucleus of the thalamus
SFO	subfornical organ
SNc	substantia nigra, compact part
SNr	substantia nigra, reticular part
SO	supraoptic nucleus
SOC	superior olivary complex
SUB	subiculum
TRS	triangular nucleus of septum
VMH	ventromedial hypothalamic nucleus
VTA	ventral tegmental area
ZI	zona incerta

contrast, the expression distribution of SST^+ neurons was quite homogeneous across cortical areas (Figures S5O–S5T). In the cortex, the PV expression level is known to be correlated with plasticity during the learning process (Donato et al., 2013). Thus, the inhomogeneity of the PV expression might reflect differences in the computation logic across different cortical areas.

From our cell-type mapping data, certain cell types were clustered in specific areas in the brain, offering clues to delineate the region boundaries. For instance, we observed that ChAT neurons were densely populated in and around the LDT (for the list of region acronyms, see Table 1). From this cluster of ChAT neurons, we defined the polygonal boundary enclosing these cells by using the alpha-shape algorithm (Figure 2I and STAR Methods). We performed the same analysis targeting TH neurons in and around the LC (Figure 2J). The polygonal boundaries defined by $ChAT^+$ and TH^+ neuron clusters were neighboring each other with a small overlap (Figure 2K). We then evaluated the overlap between polygonal boundaries using the Dice metric (STAR Methods). The result showed about 70% overlap between ChAT-ChAT and TH-TH pairs (Figure 2L). Furthermore, the overlap of the ChAT-TH pair was 2.84% ± 0.9%. These results support the accuracy of our registration method with an orthogonal evaluation metric, which is largely independent of information present in the nuclear staining channel. This result thus offers the possibility of accurately delineating the brain regions by collecting more cell-type mapping data in CUBIC-Cloud.

Last, to assess whether our analysis pipeline can accurately quantify the expression amount of the proteins, we evaluated the expression of Iba1 under an artificially induced inflammation state, because Iba1 expression is known to be correlated with microglial activation (Ito et al., 1998). In our experiment, 1 mg/kg of lipopolysaccharide (LPS), a purified extract of the outer membrane of Gram-negative bacteria, was administered to mice via intraperitoneal (i.p.) injection. The brains were sampled 24 h after injection (STAR Methods). In the isocortex, no subregions displayed significant change in the cell density ($p>0.1$,

Welch's t test, Figure S5I), whereas the mean expression amount per cell was increased significantly in all subregions ($p < 0.05$, Welch's t test, Figure S5J). The observation that cortical microglia does not proliferate, but increases its Iba1 expression upon LPS administration, was reported in Chen et al. (2012), and our results confirmed that it is globally true in all cortical areas. Outside the isocortex, most regions showed increases in Iba1 expression (Figure S5K) and had varying degrees of change. For instance, Iba1 expression amount barely changed in the cerebellum. On the other hand, we confirmed that the increase in Iba1 expression was markedly high in the SFO and IO, which are part of the circumventricular organs having a highly permeable blood-brain barrier (Furube et al., 2018).

Whole-brain analysis of Aβ plaque accumulation in an AD model mouse brain

We next applied the CUBIC-Cloud analysis framework to quantitatively understand the pathological state of the Alzheimer's disease (AD) model mouse. To demonstrate this, the whole brain from an *App*$^{NL\text{-}G\text{-}F/NL\text{-}G\text{-}F}$ AD model mouse (Saito et al., 2014) (9 to 10 months of age) was cleared and stained with anti-Aβ antibody (n = 4, STAR Methods). In LSFM images, Aβ plaques were observed as dim blobs often accompanying a bright spot at the core. On the other hand, no plaque staining pattern was observed in the control wild-type mouse brain (9 to 10 months of age, n = 3, data not shown).

We first quantified the density (number of individual plaques per volume) and the volume ratio (computed as (total plaque volume in the region)/(region volume)). In both metrics, Aβ plaque amounts were highest in the cerebral cortex and cerebral nuclei, and relatively lower amounts of plaques were observed in the brain stem and cerebellum (Figures 3A and 3B). The effective radius of the plaque (computed as $r = \{3V/(4\pi)\}^{1/3}$, where V is the plaque volume) tended to be larger in the isocortex and hippocampus and smaller in the cerebellum (Figure 3C). Within the isocortex, a relatively stronger accumulation of Aβ was observed in visual and auditory areas, whereas plaques were relatively sparse in the medial frontal areas (Figures 3D and 3E). Layer-wise abundance of Aβ plaques showed a concave profile, with its peak in layer 4 (Figure 3F). The whole-brain cartoon heatmap showing the Aβ volume ratio is shown in Figure 3G. In the brain stem, the plaque volume ratio was typically 0.5%–1.0%. Some brain-stem regions, however, showed notably larger or smaller amounts of Aβ accumulation. For example, the SNr and VMH had relatively higher amounts of Aβ compared with neighboring regions (Figures 3H and 3I). The ARH, right next to the VMH, had almost no Aβ plaques. We also observed that the regions around the ventricles showed relatively lower amounts of plaques, including TRS, DTN, MH, LH, and PVT (Figures 3G and 3J–3L).

Whole-brain analysis of c-Fos expression underlying pharmacological sleep induction by LPS

The next important application domain of CUBIC-Cloud is to reconstruct the neuronal activity profile by imaging the protein expression of immediate-early genes (IEGs) such as c-Fos. Such automated analysis would allow comprehensive identification of cellular clusters that underlie an animal's behavioral phenotype (Susaki et al., 2014; Renier et al., 2016; Tatsuki et al., 2016; Salinas et al., 2018). Reciprocally, one could define an animal's phenotype in a bottom-up manner based on the activity pattern of neuron ensembles. Here, we focused on the effect of LPS. Phenotypically, LPS induces acute sleep in mice, and we thought that IEG-based activity reconstruction would be suitable to track the relatively slow dynamics of wake-sleep cycles.

Administration of 150 μg/kg LPS to mice via i.p. injection at zeitgeber time = 14 caused an acute immune response accompanied by prolonged sleep duration, as confirmed by Snappy Sleep Stager (SSS) measurement (Figures S7A–S7C and STAR Methods). In a replicate experiment, brains were sampled 2–3 h after LPS injection, and the whole-brain c-Fos expression profile was analyzed (STAR Methods). The accuracy of the c-Fos cell detection is shown in Figure S3H. Figure 4A shows the whole-brain 3D rendering of the detected c-Fos-expressing cells (also see Table S4). We comprehensively searched for the activated or repressed brain regions by both region-wise and voxel-wise statistical analysis (Figure S7D). Our analysis revealed that c-Fos expression in some of the isocortical areas was reduced (Figures 4B and 4C), which included motor and somatosensory areas, presumably reflecting the mouse's resting state. We also found that some distinct brain nuclei were activated by LPS. Among those, the most notable regions included the BST, PVH, PVT, CEA, PB, NTS, and DMX (Figure 4D).

In our result, the specific part of the BST (the oval region; ovBST) was strongly activated by LPS (Figure 4D). Indeed, according to a recent study, the ovBST is responsible for inflammation-induced anorexia, and it receives inputs from the CEA and PB (Wang et al., 2019). Our result was able to successfully identify elevated c-Fos expression in these spatially separated yet functionally related neurons.

We also observed heterogeneous c-Fos activation in PVT. In terms of the number of c-Fos^{+} cells, the increase in number was more pronounced in the posterior PVT (pPVT) than the anterior PVT (aPVT) (Figures 4E–4G). In terms of the expression level, pPVT and aPVT showed similar levels of increase (Figures 4H and 4I). Recently, Gao et al. (Gao et al., 2020) identified two classes of distinct neurons in PVT. Type I neurons, densely located in the pPVT, respond to aversive stimuli. On the other hand, type II neurons, dominantly located in the aPVT, become silent upon aversive stimuli. It is also reported that the type II neurons are active during sleep. In the pPVT, our observation aligns with the insight of Gao, where the activated population was likely type I neurons. In the aPVT, our result might reflect the mixed response of the type II neurons, where aversive inflammatory stimuli and induced sleep were both present. It should also be noted that type I neurons in the pPVT project to the CEA, ILA, and ACB. We indeed observed that the ILA and ACB were weakly activated (Figure S7D).

Whole-brain analysis of input cells projecting to ARH^{Kiss1+} neurons

As the third application domain of CUBIC-Cloud, we show brain-wide connectivity analysis by using pseudotyped RV. To demonstrate this application, we focused on a population of neurons that secrete kisspeptin (a neuropeptide encoded by the *Kiss1*

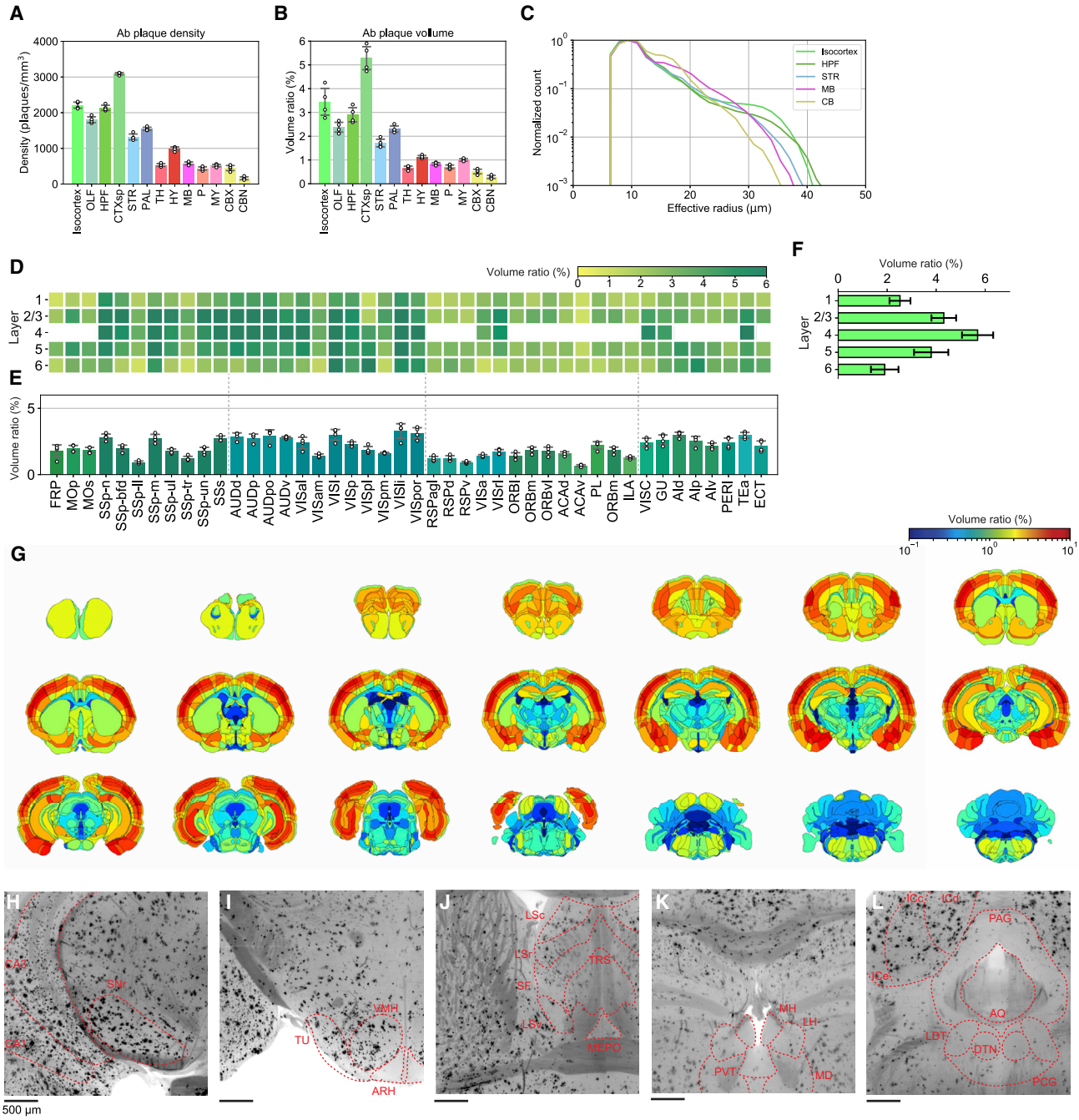

Figure 3. Whole-brain analysis of Aβ plaque accumulation in an AD model mouse brain

Using the *App*NL-G-F/NL-G-F AD model mouse brain (9 to 10 months of age), brain-wide accumulation of Aβ plaques was quantified by applying whole-mount 3D immunostaining and by using the CUBIC-Cloud analysis framework.

(A) Density of Aβ plaques (number of plaques/mm^3) in major brain divisions (n = 4). Data are shown as the mean ± SD (n = 4).

(B) Volume ratio of Aβ plaques in major brain divisions (n = 4), computed as (total plaque volume in the region)/(region volume). Data are shown as the mean ± SD (n = 4).

(C) Distribution of effective radius of Aβ plaques in the isocortex, hippocampus (HPF), striatum (STR), midbrain (MB), and cerebellum (CB) (n = 4).

(D and E) The volume ratio of Aβ plaques in the isocortex (n = 4). In (E), data are shown as the mean ± SD.

(F) Layer-wise average of (D). Data are shown as the mean ± SD (n = 4).

(G) Cartoon heatmaps showing the Aβ plaque volume ratio in each brain region (n = 4).

(H–L) Raw 6E10 immunostaining images around SNr (H), VMH (I), TRS and MEPO (J), LDT and DTN (K), and MH, LH, and PVT (L).

CellPress
OPEN ACCESS

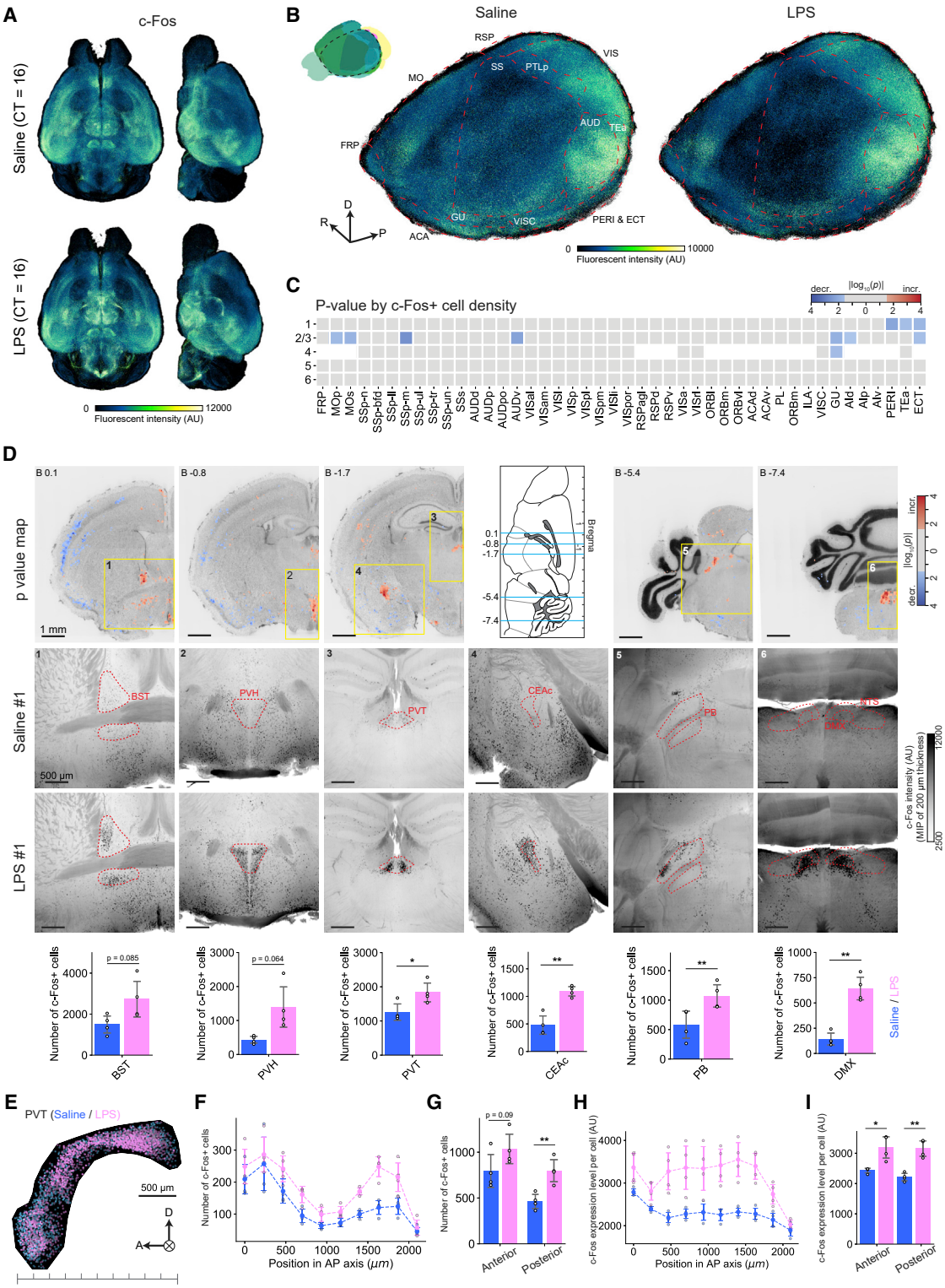

Figure 4. Whole-brain analysis of c-Fos expression level changes by LPS administration

LPS acutely induces sleep in mice. Brain-wide neural activity change induced by LPS was quantified by applying whole-mount 3D immunostaining of c-Fos and by using the CUBIC-Cloud analysis framework.

(A) Whole-brain views of all c-Fos$^+$ cells, showing saline- (top) and LPS- (bottom) administered brains. Each point (i.e., single cell) was assigned a pseudo-color based on its fluorescence intensity.

(legend continued on next page)

gene) located in the ARH, hereafter termed as ARH^{Kiss1+}. Those neurons were shown to play an important role in reproduction behavior in mammals by regulating pulsatile release of gonadotrophin-releasing hormone at around 0.3 to 1.0 pulses per hour (Herbison, 2018). Intriguingly, the pulse frequency changes through the estrus cycle in females, but not in males. As such, we comprehensively investigated the neural inputs to ARH^{Kiss1+} neurons to search the mechanism of pulse generation/modulation on the basis of neural circuitry.

To achieve cell-type-specific targeting of virus infection, we used the Cre/*loxP* system and RV transsynaptic tracing combined with Cre-dependent AAV vectors (Miyamichi et al., 2013) (Figure 5A and STAR Methods). After virus injection, brains (both male and female) were cleared by CUBIC reagents and analyzed by CUBIC-Cloud pipeline (STAR Methods). We first checked the distribution of starter cells (GFP$^+$ and mCherry$^+$) to ensure that the injection was successful and the starter cells were well confined within the ARH (Figure 5B). In the present study, the criterion for selecting successful samples was defined as more than 45% of starter cells localized in the ARH or PVp. (Note that the area annotated as PVp in the Allen Brain Atlas belongs to a part of the ARH in the Paxinos atlas; Paxinos and Franklin, 2012.) With this criterion, of 20 injections, n = 3 and n = 4 brains were assessed as successful for male and female, respectively (Figure 5B).

Figure 5C shows the whole-brain overview of all input (GFP$^+$ and mCherry$^-$) cells. The accuracy of the GFP$^+$ cell detection is shown in Figure S3B. Our quantitative analysis identified $(3.1 \pm 0.5) \times 10^4$ input cells in the male brain (n = 3), the majority of which (>85%) were located within the hypothalamus (Figure 5D and Table S5). As is shown in Figure 5E, ARH^{Kiss1+} neurons receive inputs from dozens of discrete structures throughout the forebrain and brain stem, including the striatum (LS), pallidum (BST), thalamus (PVT), hypothalamus (MPO, MPN, AHN, PVH, DMH, VMH, and PH), hippocampal formation (HATA and SUB), midbrain (MRN and PAG), and pons (PB). Remarkably, extremely sparse populations, only a few dozens of cells per region, were reproducibly identified (Figures 5F and 5G). In terms of cell density, those populations were often equivalent to less than 10 cells/mm^3, which could be easily overlooked with slice-based approaches. These sparse populations were not reported in the past literature (Yeo et al., 2019).

We next performed statistical analysis comparing the number of input cells between male and female brains (STAR Methods). Overall, binary connectivity differences (i.e., zero in one sex and some finite number in the other sex) were not observed (Figure S8A). Weak differences were suggested in LS, MPO, MPN, and AVP (Figures S8B–S8H and STAR Methods), which are neighbors to one another. The difference was most pronounced in the LSr, which is known to inhibit the lordosis behavior during mating interactions (Tsukahara et al., 2014). The sexually dimorphic circuit from LSr to PAG is reported, where female brains contain more neurons in the LSr that project to the PAG (Tsukahara and Yamanouchi, 2002). Our results suggest that LSr sends sexually dimorphic projections to ARH^{Kiss1+}. The identities of these populations can be fully characterized in future studies.

DISCUSSION

In this study, we presented an integrated computational framework for single-cell-resolution whole-brain analysis, named CUBIC-Cloud. Inspired by the scientific data platforms developed in genomics, we postulated that the framework should provide (1) a reference brain atlas and automatic mapping to the reference, (2) open opportunities for the research community to contribute new data, (3) a toolkit to visualize and quantify data, and (4) easy and universal accessibility. As we have shown in this study, CUBIC-Cloud addressed these requirements by designing a new software stack embracing the latest cloud technologies, widely available for researchers in neuroscience (Figure 1). Users can access CUBIC-Cloud at https://cubic-cloud.com.

After describing the software infrastructures offered by CUBIC-Cloud, we extensively evaluated and validated the accuracy and reproducibility of the proposed framework by various applications. First, we quantified the exact number of various cell types, including PV-, SST-, ChAT-, TH-, and Iba1-expressing cells (Figure 2). We were surprised by the small variation between individual animals in terms of labeled cell numbers (quantified SD usually less than 10%), which not only highlighted the accuracy of our analysis but also implied the intricate regulation of cell proliferation in the brain. We further showed that CUBIC-Cloud can also be used to quantitatively understand the pathological state of the AD model mouse (Figure 3). Together, these demonstrations encourage the future application of CUBIC-Cloud to construct datasets of disease models and drug effects, where decreases or increases in particular markers in specific brain regions might correlate with disease progression.

(B) Magnified 3D views of (A), where the left isocortex is selectively displayed. Orientation arrows stand for R (right), D (dorsal), and P (posterior).
(C) A p value heatmap showing the isocortex regions whose c-Fos$^+$ cell density was significantly affected by LPS (n = 4 each). The p value was computed by comparing the c-Fos$^+$ cell count. The color lookup table is log scaled (base 10), where red represents the regions that were activated (i.e., more c-Fos$^+$ cells) by LPS, and blue represents the repressed regions. Regions with no statistical significance ($p > 0.05$) were assigned a gray color.
(D) Distinct brain regions activated by LPS (n = 4 each). The top row shows the voxel-wise p value map. Color lookup table follows that of (C). The second and third rows are the raw c-Fos images of saline- and LPS-administered groups, respectively. The fourth row shows the number of c-Fos$^+$ cells of the identified regions. Data are shown and mean ± SD (n = 4).
(E) Plot of c-Fos$^+$ cells in PVT. Cells are pseudo-colored with their intensity values. Pink (blue) dots are from LPS (saline)-administered brains, respectively.
(F) The number of c-Fos$^+$ cells in the PVT in 10 divisions along the anterior-posterior (AP) axis. Data are shown and mean ± SD (n = 4).
(G) The number of c-Fos$^+$ cells in the anterior and posterior half of the PVT. The boundary between anterior and posterior regions was set at the center of the PVT along the AP axis. Data are shown and mean ± SD (n = 4).
(H) The c-Fos expression levels per cell in the PVT, 10 divisions along the AP axis. Data are shown and mean ± SD (n = 4).
(I) The c-Fos expression levels per cell in the anterior and posterior halves of the PVT. Data are shown and mean ± SD (n = 4). *p<0.05, **p<0.01, Welch's t test.
Brain region acronyms follow the ontology defined by the Allen Brain Atlas.

CellPress
OPEN ACCESS

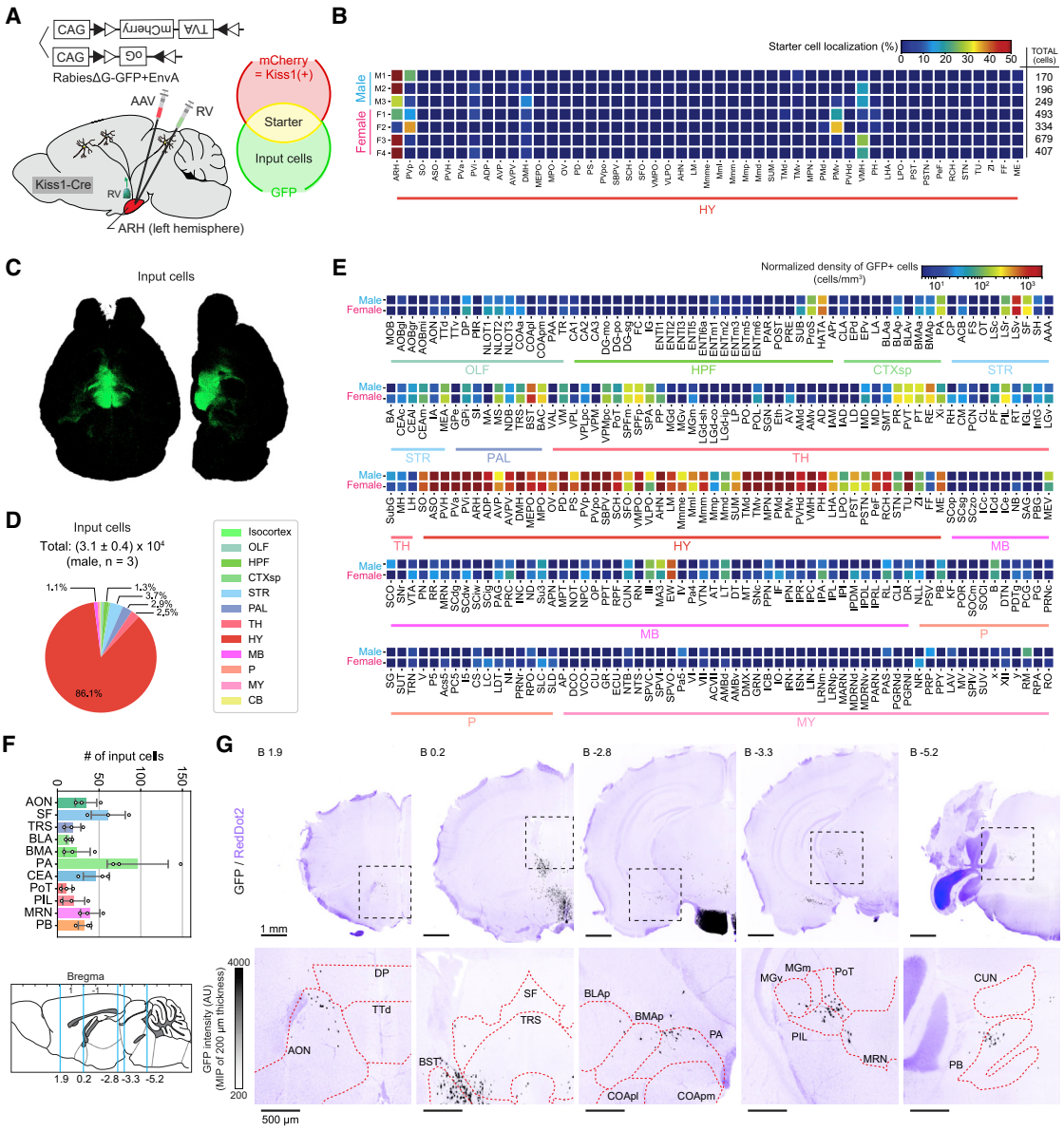

Figure 5. Whole-brain analysis of input cell populations projecting to ARH^{Kiss1+} neurons

(A) Virus injection scheme. AAV carrying mCherry, TVA receptor, and optimized glycoprotein (oG) was injected into the ARH of Kiss1-Cre transgenic mouse, followed by injection of modified rabies virus carrying GFP. Cells expressing both mCherry and GFP are the starter cells.

(B) Quantification of starter cell localization. The ratio was computed by dividing the cell count in each region by the total number of starter cells. The total number of starter cells in each sample is shown on the right end of the heatmap.

(C) Whole-brain view of all input cells.

(D) Total cell count and the distribution of input cells. Only male brains were considered here.

(E) Cell-density heatmap of all brain regions (excluding the isocortex and cerebellum, where virtually no input cells were detected). The means of male and female brains are shown.

(F) The plot shows extremely sparse input cell populations in previously unidentified brain regions (n = 3). Only male brains were considered here. Data are shown and mean ± SD (n = 3).

(G) Raw GFP (black) and nuclear staining (RedDot2, purple) images showing the regions identified in (F). Macro views (top) and zoomed-in views (of boxed areas; bottom) are shown. Brain region acronyms follow the ontology defined by the Allen Brain Atlas.

We have also explored the application of CUBIC-Cloud to reconstruct a whole-brain neuronal activity profile by using c-Fos immunostaining. Our whole-brain analysis showed that administration of LPS, which induces sleepiness, repressed the c-Fos expression in some of the cortical areas, whereas it activated several distinct brain regions (Figure 4). For example,

our analysis revealed that a distinct subpopulation in the ovBST strongly responded to LPS, and that the response in PVT neurons is heterogeneous. CUBIC-Cloud facilitates sharing such knowledge through a widely accessible data repository, and users will know exactly, with $\leq$100 μm spatial resolution in 3D space, where the relevant region is. By iterating such experiments, CUBIC-Cloud opens up the possibility of functionally dissecting the mouse brain with much finer detail and specificity.

Furthermore, CUBIC-Cloud was used to comprehensively identify brain-wide neuronal connections. As a proof-of-concept demonstration, input of neuronal populations projecting to ARH^{Kiss1+} neurons was investigated by using RV tracers (Figure 5). Our analysis was successful in identifying extremely sparse populations (less than 10 cells/mm^3) with high reproducibility. Our results also implied sexually dimorphic projection from LSr to ARH^{Kiss1+}. Again, we emphasize that CUBIC-Cloud can serve as a central hub for researchers to share such anatomical knowledge.

The above analysis results are all openly accessible at CUBIC-Cloud. The raw image data, along with the markers highlighting the detected cells, are available through the CATMAID image browser (Saalfeld et al., 2009), hosted at http://cubic-atlas.riken.jp.

Open data sharing and reanalysis have been highly successful in neuroscience over the past decade. For instance, NeuroMorpho.org (Ascoli et al., 2007) is a community-driven storage for single-neuron reconstructions, which now hosts over 100,000 curated cells. NeuroData.io (Vogelstein et al., 2018) is another initiative for sharing neuroscientific data, primarily focused on sharing the large raw image files through the cloud. CUBIC-Cloud serves a distinct role among these resources, by focusing its mission on the whole mouse brain dataset, represented as a cellular point cloud. We believe that all these cloud services are complementary to each other. Namely, researchers can submit the curated point-cloud data in CUBIC-Cloud, and the raw image data can be deposited in NeuroData.io. A smooth and coherent integration of these services via public API would be beneficial in future developments.

CUBIC-Cloud has pioneered the cloud-based framework to share and publish whole mouse-brain datasets. We believe, however, that several technical and administrative advancements need to be made to render it a fully functional and user-friendly scientific data platform for neuroscience. First, the current implementation of CUBIC-Cloud asks the user to perform cell detection locally. The cell (object) detection routine, along with the machine learning training, should be integrated into the cloud in future developments. Indeed, there are already several reports on embracing cloud computing to analyze massive light and electron microscopy images (Haberl et al., 2018; Falk et al., 2019; Bannon et al., 2019; Wu et al., 2019). An interesting bonus of running object detection in the cloud is that the training datasets can also be shared, which will allow the training of more general and accurate deep learning models (Bannon et al., 2019). Furthermore, CUBIC-Cloud is currently aimed at analyzing single-cell-resolution image data, where signals of interest are given as dots localized in cell nuclei/soma. Inclusion of an object detection routine in the cloud would expand the scope to include fiber and synaptic structures. Technically, such high-resolution image data can be readily obtained by state-of-the-art LSFM, and resolution can be boosted by expansion microscopy (Chen et al., 2015; Ku et al., 2016; Tomer et al., 2014; Murakami et al., 2018). Future software infrastructure developments, including ones discussed here, will pave the way for new science toward bottom-up and data-driven elucidation of neuronal functions and circuitry.

Limitations of the study

CUBIC-Cloud has been rigorously tested and validated with the CUBIC clearing method by registering over 50 brains. CUBIC-Cloud should be compatible with clearing methods with similar tissue deformation characteristics (e.g., hydrophilic clearing methods, which often soften and expand the tissue). However, we found that the registration accuracy was compromised, especially in the olfactory bulb, when iDISCO, a hydrophobic clearing method, was used (Figure S4 and STAR Methods). The current registration algorithm cannot correctly overcome the large deformation present in the olfactory bulb, and calls for future work.

Using CUBIC-Cloud, we were able to quantify the number of cells labeled by immunostaining and the protein abundance levels. As quantified in Figure S2, however, the fluorescence intensity from deeper brain regions such as the thalamus was attenuated by a factor of around 2, due to the absorption and residual scattering of the tissue. A certain calibration process would be ideally required to correct the intensity attenuation in the deep brain regions. Using tissue-embedded beads could be a possible solution, but the bead aggregation might complicate the automatic calibration. As an alternative solution, we think that a nuclear staining channel could be used to calibrate the intensity. Assuming that all cells have a single copy of DNA in the nucleus, the brightness of the nuclear staining of single cells would be almost the same. Furthermore, the absolute density of the cells of all brain areas is available from CUBIC-Atlas. Given this, one might compute the correction factor by dividing the raw image intensity of nuclear staining by the cell density. Although we have not implemented this analysis in our pipeline, ideas along this line would be useful in future studies.

The proposed whole-brain analysis and sharing pipeline was specifically designed for mouse brain studies. However, given that tissue-clearing-based high-throughput imaging is applicable to exploring the brains of rarely explored organisms (Pende et al., 2020), it would be important to extend the framework in the future to accommodate the brains of other organisms, such as rats or primates. As the whole-brain data of diverse organisms are collected, we expect that a data integration platform like CUBIC-Cloud would further increase its value.

STAR★METHODS

Detailed methods are provided in the online version of this paper and include the following:

- KEY RESOURCES TABLE
- RESOURCE AVAILABILITY
  - Lead contact
  - Materials availability
  - Data and code availability

SUPPLEMENTAL INFORMATION

Supplemental information can be found online at https://doi.org/10.1016/j.crmeth.2021.100038.

ACKNOWLEDGMENTS

The authors would like to thank K. Wilkins and T. Miyawaki for proofreading the manuscript, T.C. Murakami for discussions on CUBIC-Atlas, M. Kuroda for technical assistance on LSFM imaging, S.I. Kubota for helping with the LPS experiments, and R. Tanaka for supporting sample preparations. The *App*$^{NL-G-F/NL-G-F}$ knockin mouse strain (RBRC06344) was provided by RIKEN BRC (deposited by T. Saito and T.C. Saido) through the National BioResource Project of the MEXT/AMED, Japan. This work was supported by a Grant-in-Aid for JSPS Fellows (JSPS KAKENHI, grant 19J13071, to T.M.); an ANRI scholarship (to T.M.); PRESTO (JST, grant JPMJPR15F4, to E.A.S.); a Grant-in-Aid for Scientific Research (B) (JSPS KAKENHI, grant 19H03413 to E.A.S.); a Grant-in-Aid for Scientific Research on Innovative Areas (JSPS KAKENHI, grant 17H06328 to E.A.S.); AMED-PRIME (JP21gm6210027, to E.A.S.); ERATO Touhara Chemosensory Signal Project (JST, grant JPMJER1202, to K.T.); a Grant-in-Aid for Scientific Research (S) (JSPS KAKENHI, grant 25221004, to H.R.U.); Brain/MINDS (AMED/MEXT, grant JP17DM0207049, to H.R.U.); the Science and Technology Platform Program for Advanced Biological Medicine (AMED/MEXT to H.R.U.); a Grant-in-Aid from the Human Frontier Science Program (to H.R.U.); and Grants-in-Aid from the Takeda Science Foundation (to E.A.S. and H.R.U.). The graphical user interface of CUBIC-Cloud was co-developed by CUBICStars and Tecotec, Inc.

AUTHOR CONTRIBUTIONS

T.M. and H.R.U. designed the study. T.M. created and implemented the CUBIC-Cloud software stack. T.M. and K.K. performed data analysis. T.M. and E.A.S. performed LSFM imaging. C.S., K.K., and H.O. performed tissue clearing and immunostaining experiments. K.K. performed sleep measurements by using SSS. H.O. assisted in the preparation of AD model mice. S.S. and R.G.Y. assisted in the deployment of the cloud server. E.A.S., K.T., K. Murata, and K. Miyamichi prepared Cre-mice, produced virus, and performed injections. T.M., S.S., and H.R.U. wrote the manuscript with input from all co-authors.

DECLARATION OF INTERESTS

T.M., R.G.Y., and E.A.S are employees of CUBICStars, Inc. H.R.U. is a founder and CTO of CUBICStars, Inc. T.M. and H.R.U. are co-inventors on patent applications filed by CUBICStars, Inc., regarding the CUBIC-Cloud framework. CUBIC-Cloud web service is provided and maintained by CUBICStars, Inc. H.R.U. is a co-inventor on patents and patent applications owned or filed by RIKEN covering the CUBIC reagents.

Received: December 21, 2020
Revised: March 17, 2021
Accepted: May 20, 2021
Published: June 21, 2021

REFERENCES

Adzic, G., and Chatley, R. (2017). Serverless computing: economic and architectural impact. In Proceedings of the 2017 11th Joint Meeting on Foundations of Software Engineering - ESEC/FSE (ACM Press), pp. 884–889.

Armstrong, D.M., Saper, C.B., Levey, A.I., Wainer, B.H., and Terry, R.D. (1983). Distribution of cholinergic neurons in rat brain: demonstrated by the immunocytochemical localization of choline acetyltransferase. J. Comp. Neurol. *216*, 53–68.

Ascoli, G.A., Donohue, D.E., and Halavi, M. (2007). NeuroMorpho.Org: a central resource for neuronal morphologies. J. Neurosci. *27*, 9247–9251.

Avants, B.B., Epstein, C.L., Grossman, M., and Gee, J.C. (2008). Symmetric diffeomorphic image registration with cross-correlation: evaluating automated labeling of elderly and neurodegenerative brain. Med. Image Anal. *12*, 26–41.

Bannon, D., Moen, E., Schwartz, M., Borba, E., Cui, S., Huang, K., Camplisson, I., Koe, N., Kyme, D., Kudo, T., et al. (2019). Dynamic allocation of computational resources for deep learning-enabled cellular image analysis with Kubernetes. bioRxiv, 505032.

Belle, M., Godefroy, D., Couly, G., Malone, S.A., Collier, F., Giacobini, P., and Chédotal, A. (2017). Tridimensional visualization and analysis of early human development. Cell *169*, 161–173.e12.

Berg, S., Kutra, D., Kroeger, T., Straehle, C.N., Kausler, B.X., Haubold, C., Schiegg, M., Ales, J., Beier, T., Rudy, M., et al. (2019). ilastik: interactive machine learning for (bio)image analysis. Nat. Methods *4522*, 3–5.

Cai, R., Pan, C., Ghasemigharagoz, A., Todorov, M.I., Förstera, B., Zhao, S., Bhatia, H.S., Parra-Damas, A., Mrowka, L., Theodorou, D., et al. (2019). Panoptic imaging of transparent mice reveals whole-body neuronal projections and skull–meninges connections. Nat. Neurosci. *22*, 317–327.

Celio, M. (1990). Calbindin D-28k and parvalbumin in the rat nervous system. Neuroscience *35*, 375–475.

Chan, K.Y., Jang, M.J., Yoo, B.B., Greenbaum, A., Ravi, N., Wu, W.L., Sánchez-Guardado, L., Lois, C., Mazmanian, S.K., Deverman, B.E., and Gradinaru, V. (2017). Engineered AAVs for efficient noninvasive gene delivery to the central and peripheral nervous systems. Nat. Neurosci. *20*, 1172–1179.

Chen, Z., Jalabi, W., Shpargel, K.B., Farabaugh, K.T., Dutta, R., Yin, X., Kidd, G.J., Bergmann, C.C., Stohlman, S.A., and Trapp, B.D. (2012). Lipopolysaccharide-induced microglial activation and neuroprotection against experimental brain injury is independent of hematogenous TLR4. J. Neurosci. *32*, 11706–11715.

Chen, F., Tillberg, P.W., and Boyden, E.S. (2015). Expansion microscopy. Science *347*, 543–548.

Chung, K., Wallace, J., Kim, S.-Y., Kalyanasundaram, S., Andalman, A.S., Davidson, T.J., Mirzabekov, J.J., Zalocusky, K.A., Mattis, J., Denisin, A.K., et al. (2013). Structural and molecular interrogation of intact biological systems. Nature *497*, 332–337.

Dahlström, A., and Fuxe, K. (1964). Evidence for the existence of monoamine-containing neurons in the central nervous system. I. Demonstration of monoamines in the cell bodies of brain stem neurons. Acta Physiol. Scand. Suppl. *39* (*Suppl 232*), 1–55.

Dodt, H.-U., Leischner, U., Schierloh, A., Jährling, N., Mauch, C.P., Deininger, K., Deussing, J.M., Eder, M., Zieglgänsberger, W., and Becker, K. (2007). Ultramicroscopy: three-dimensional visualization of neuronal networks in the whole mouse brain. Nat. Methods *4*, 331–336.

Donato, F., Rompani, S.B., and Caroni, P. (2013). Parvalbumin-expressing basket-cell network plasticity induced by experience regulates adult learning. Nature *504*, 272–276.

Ertürk, A., Becker, K., Jährling, N., Mauch, C.P., Hojer, C.D., Egen, J.G., Hellal, F., Bradke, F., Sheng, M., and Dodt, H.-U. (2012). Three-dimensional imaging of solvent-cleared organs using 3DISCO. Nat. Protoc. *7*, 1983–1995.

Falk, T., Mai, D., Bensch, R., Çiçek, Ö., Abdulkadir, A., Marrakchi, Y., Böhm, A., Deubner, J., Jäckel, Z., Seiwald, K., et al. (2019). U-Net: deep learning for cell counting, detection, and morphometry. Nat. Methods *16*, 67–70.

Frasconi, P., Silvestri, L., Soda, P., Cortini, R., Pavone, F.S., and Iannello, G. (2014). Large-scale automated identification of mouse brain cells in confocal light sheet microscopy images. Bioinformatics *30*, i587–i593.

Fu, Q., Martin, B.L., Matus, D.Q., and Gao, L. (2016). Imaging multicellular specimens with real-time optimized tiling light-sheet selective plane illumination microscopy. Nat. Commun. *7*, 11088.

Fürth, D., Vaissière, T., Tzortzi, O., Xuan, Y., Märtin, A., Lazaridis, I., Spigolon, G., Fisone, G., Tomer, R., Deisseroth, K., et al. (2018). An interactive framework for whole-brain maps at cellular resolution. Nat. Neurosci. *21*, 139–149.

Furube, E., Kawai, S., Inagaki, H., Takagi, S., and Miyata, S. (2018). Brain region-dependent heterogeneity and dose-dependent difference in transient microglia population increase during lipopolysaccharide-induced inflammation. Sci. Rep. *8*, 1–15.

Gao, L. (2015). Extend the field of view of selective plan illumination microscopy by tiling the excitation light sheet. Opt. Express *23*, 6102.

Gao, C., Leng, Y., Ma, J., Rooke, V., Rodriguez-Gonzalez, S., Ramakrishnan, C., Deisseroth, K., and Penzo, M.A. (2020). Two genetically, anatomically and functionally distinct cell types segregate across anteroposterior axis of paraventricular thalamus. Nat. Neurosci. *23*, 217–228.

Gonchar, Y., Wang, Q., and Burkhalter, A. (2007). Multiple distinct subtypes of GABAergic neurons in mouse visual cortex identified by triple immunostaining. Front. Neuroanat. *1*, 3.

Gradinaru, V., Treweek, J., Overton, K., and Deisseroth, K. (2018). Hydrogel-tissue chemistry: principles and applications. Annu. Rev. Biophys. *47*, 355–376.

Haberl, M.G., Churas, C., Tindall, L., Boassa, D., Phan, S., Bushong, E.A., Madany, M., Akay, R., Deerinck, T.J., Peltier, S.T., and Ellisman, M.H. (2018). CDeep3M—Plug-and-Play cloud-based deep learning for image segmentation. Nat. Methods *15*, 677–680.

Hama, H., Kurokawa, H., Kawano, H., Ando, R., Shimogori, T., Noda, H., Fukami, K., Sakaue-Sawano, A., and Miyawaki, A. (2011). Scale: a chemical approach for fluorescence imaging and reconstruction of transparent mouse brain. Nat. Neurosci. *14*, 1481–1488.

Hama, H., Hioki, H., Namiki, K., Hoshida, T., Kurokawa, H., Ishidate, F., Kaneko, T., Akagi, T., Saito, T., Saido, T., and Miyawaki, A. (2015). ScaleS: an optical clearing palette for biological imaging. Nat. Neurosci. *18*, 1518–1529.

Herbison, A.E. (2018). The Gonadotropin-releasing hormone pulse generator. Endocrinology *159*, 3723–3736.

Ito, D., Imai, Y., Ohsawa, K., Nakajima, K., Fukuuchi, Y., and Kohsaka, S. (1998). Microglia-specific localisation of a novel calcium binding protein, Iba1. *Brain research*. Mol. Brain Res. *57*, 1–9.

Johansson, O., Hökfelt, T., and Elde, R. (1984). Immunohistochemical distribution of somatostatin-like immunoreactivity in the central nervous system of the adult rat. Neuroscience *13*, 265–IN2.

Karolchik, D., Hinrichs, A.S., and Kent, W.J. (2009). The UCSC Genome Browser. Curr. Protocols Bioinformatics, Chapter 1:Unit1.4.

Ke, M.-T., Fujimoto, S., and Imai, T. (2013). SeeDB: a simple and morphology-preserving optical clearing agent for neuronal circuit reconstruction. Nat. Neurosci. *16*, 1154–1161.

Kim, E.J., Jacobs, M.W., Ito-Cole, T., and Callaway, E.M. (2016). Improved monosynaptic neural circuit tracing using engineered rabies virus glycoproteins. Cell Rep. *15*, 692–699.

Kim, Y., Yang, G.R., Pradhan, K., Venkataraju, K.U., Bota, M., García del Molino, L.C., Fitzgerald, G., Ram, K., He, M., Levine, J.M., et al. (2017). Brain-wide maps reveal stereotyped cell-type-based cortical architecture and subcortical sexual dimorphism. Cell *171*, 456–469.e22.

Kirst, C., Skriabine, S., Vieites-Prado, A., Topilko, T., Bertin, P., Gerschenfeld, G., Verny, F., Topilko, P., Michalski, N., Tessier-Lavigne, M., and Renier, N. (2020). Mapping the fine-scale organization and plasticity of the brain vasculature. Cell *180*, 780–795.e25.

Ku, T., Swaney, J., Park, J.-Y., Albanese, A., Murray, E., Cho, J.H., Park, Y.-G., Mangena, V., Chen, J., and Chung, K. (2016). Multiplexed and scalable super-resolution imaging of three-dimensional protein localization in size-adjustable tissues. Nat. Biotechnol. *34*, 973–981.

Kubota, S.I., Takahashi, K., Nishida, J., Morishita, Y., Ehata, S., Tainaka, K., Miyazono, K., and Ueda, H.R. (2017). Whole-body profiling of cancer metastasis with single-cell resolution. Cell Rep. *20*, 236–250.

Li, X., Yu, B., Sun, Q., Zhang, Y., Ren, M., Zhang, X., Li, A., Yuan, J., Madisen, L., Luo, Q., et al. (2018). Generation of a whole-brain atlas for the cholinergic system and mesoscopic projectome analysis of basal forebrain cholinergic neurons. Proc. Natl. Acad. Sci. U SA *115*, 415–420.

Mano, T., Albanese, A., Dodt, H.-U., Erturk, A., Gradinaru, V., Treweek, J.B., Miyawaki, A., Chung, K., and Ueda, H.R. (2018). Whole-brain analysis of cells and circuits by tissue clearing and light-sheet microscopy. J. Neurosci. *38*, 9330–9337.

Matsumoto, K., Mitani, T.T., Horiguchi, S.A., Kaneshiro, J., Murakami, T.C., Mano, T., Fujishima, H., Konno, A., Watanabe, T.M., Hirai, H., and Ueda, H.R. (2019). Advanced CUBIC tissue clearing for whole-organ cell profiling. Nat. Protoc. *14*, 3506–3537.

McDonald, A., and Betette, R. (2001). Parvalbumin-containing neurons in the rat basolateral amygdala: morphology and co-localization of Calbindin-D28k. Neuroscience *102*, 413–425.

Miyamichi, K., Shlomai-Fuchs, Y., Shu, M., Weissbourd, B.C., Luo, L., and Mizrahi, A. (2013). Dissecting local circuits: parvalbumin Interneurons underlie broad feedback control of olfactory bulb output. Neuron *80*, 1232–1245.

Murakami, T.C., Mano, T., Saikawa, S., Horiguchi, S.A., Shigeta, D., Baba, K., Sekiya, H., Shimizu, Y., Tanaka, K.F., Kiyonari, H., et al. (2018). A three-dimensional single-cell-resolution whole-brain atlas using CUBIC-X expansion microscopy and tissue clearing. Nat. Neurosci. *21*, 625–637.

Murray, E., Cho, J.H., Goodwin, D., Ku, T., Swaney, J., Kim, S.-Y., Choi, H., Park, Y.-G., Park, J.-Y., Hubbert, A., et al. (2015). Simple, scalable Proteomic imaging for high-dimensional profiling of intact systems. Cell *163*, 1500–1514.

Osakada, F., and Callaway, E.M. (2013). Design and generation of recombinant rabies virus vectors. Nat. Protoc. *8*, 1583–1601.

Paxinos, G., and Franklin, K. (2012). Paxinos and Franklin's the Mouse Brain in Stereotaxic Coordinates, 4th Edition (Academic Press).

Pende, M., Vadiwala, K., Schmidbaur, H., Stockinger, A.W., Murawala, P., Saghafi, S., Dekens, M.P.S., Becker, K., Revilla-i Domingo, R., Papadopoulos, S.-C., et al. (2020). A versatile depigmentation, clearing, and labeling method for exploring nervous system diversity. Sci. Adv. *6*, eaba0365.

Potree, M.S. (2016). Rendering Large Point Clouds in Web Browsers, PhD thesis.

Power, R.M., and Huisken, J. (2017). A guide to light-sheet fluorescence microscopy for multiscale imaging. Nat. Methods *14*, 360–373.

Renier, N., Wu, Z., Simon, D.J., Yang, J., Ariel, P., and Tessier-Lavigne, M. (2014). iDISCO: a simple, rapid method to immunolabel large tissue samples for volume imaging. Cell *159*, 896–910.

Renier, N., Adams, E.L., Kirst, C., Wu, Z., Azevedo, R., Kohl, J., Autry, A.E., Kadiri, L., Umadevi Venkataraju, K., Zhou, Y., et al. (2016). Mapping of brain activity by automated volume Analysis of immediate early genes. Cell *165*, 1789–1802.

Saalfeld, S., Cardona, A., Hartenstein, V., and Tomancak, P. (2009). CATMAID: collaborative annotation toolkit for massive amounts of image data. Bioinformatics (Oxford, England) *25*, 1984–1986.

Saito, T., Matsuba, Y., Mihira, N., Takano, J., Nilsson, P., Itohara, S., Iwata, N., and Saido, T.C. (2014). Single App knock-in mouse models of Alzheimer's disease. Nat. Neurosci. *17*, 661–663.

Salinas, C.B.G., Lu, T.T.-H., Gabery, S., Marstal, K., Alanentalo, T., Mercer, A.J., Cornea, A., Conradsen, K., Hecksher-Sørensen, J., Dahl, A.B., et al. (2018). Integrated brain atlas for unbiased mapping of nervous system effects following Liraglutide treatment. Scientific Rep. *8*, 10310.

Sommer, C., Straehle, C., Kothe, U., and Ilastik, F.A.H. (2011). Interactive learning and segmentation toolkit. IEEE International Symposium on Biomedical Imaging: From Nano to Macro (IEEE), pp. 230–233.

Sunagawa, G.A., Sumiyama, K., Ukai-Tadenuma, M., Perrin, D., Fujishima, H., Ukai, H., Nishimura, O., Shi, S., Ohno, R.-i., Narumi, R., et al. (2016). Mammalian reverse Genetics without crossing reveals Nr3a as a short-sleeper gene. Cell Rep. *14*, 662–677.

Susaki, E.A., and Ueda, H.R. (2016). Whole-body and whole-organ clearing and imaging techniques with single-cell resolution: toward organism-level systems biology in mammals. Cell Chem. Biol. *23*, 137–157.

Susaki, E.A., Tainaka, K., Perrin, D., Kishino, F., Tawara, T., Watanabe, T.M., Yokoyama, C., Onoe, H., Eguchi, M., Yamaguchi, S., et al. (2014). Whole-brain imaging with single-cell resolution using chemical Cocktails and computational analysis. Cell *157*, 726–739.

Susaki, E.A., Tainaka, K., Perrin, D., Yukinaga, H., Kuno, A., and Ueda, H.R. (2015). Advanced CUBIC protocols for whole-brain and whole-body clearing and imaging. Nat. Protoc. *10*, 1709–1727.

Susaki, E.A., Shimizu, C., Kuno, A., Tainaka, K., Li, X., Nishi, K., Morishima, K., Ono, H., Ode, K.L., Saeki, Y., et al. (2020). Versatile whole-organ/body staining and imaging based on electrolyte-gel properties of biological tissues. Nat. Commun. *11*, 1982.

Tainaka, K., Kubota, S.I., Suyama, T.Q., Susaki, E.A., Perrin, D., Ukai-Tadenuma, M., Ukai, H., and Ueda, H.R. (2014). Whole-body imaging with single-cell resolution by tissue Decolorization. Cell *159*, 911–924.

Tainaka, K., Kuno, A., Kubota, S.I., Murakami, T., and Ueda, H.R. (2016). Chemical Principles in tissue clearing and staining protocols for whole-body cell profiling. Annu. Rev. Cell Dev. Biol. *32*, 713–741.

Tainaka, K., Murakami, T.C., Susaki, E.A., Shimizu, C., Saito, R., Takahashi, K., Hayashi-Takagi, A., Sekiya, H., Arima, Y., Nojima, S., et al. (2018). Chemical landscape for tissue clearing based on hydrophilic reagents. Cell Rep. *24*, 2196–2210.e9.

Tatsuki, F., Sunagawa, G.A., Shi, S., Susaki, E.A., Yukinaga, H., Perrin, D., Sumiyama, K., Ukai-Tadenuma, M., Fujishima, H., Ohno, R.-i., et al. (2016). Involvement of Ca 2+ -dependent Hyperpolarization in sleep duration in mammals. Neuron *90*, 70–85.

Tomer, R., Ye, L., Hsueh, B., and Deisseroth, K. (2014). Advanced CLARITY for rapid and high-resolution imaging of intact tissues. Nat. Protoc. *9*, 1682–1697.

Tsukahara, S., and Yamanouchi, K. (2002). Sex difference in septal neurons projecting axons to midbrain central gray in rats: a combined Double retrograde tracing and ER-immunohistochemical study. Endocrinology *143*, 285–294.

Tsukahara, S., Kanaya, M., and Yamanouchi, K. (2014). Neuroanatomy and sex differences of the lordosis-inhibiting system in the lateral septum. Front. Neurosci. *8*, 1–13.

Vogelstein, J.T., Perlman, E., Falk, B., Baden, A., Gray Roncal, W., Chandrashekhar, V., Collman, F., Seshamani, S., Patsolic, J.L., Lillaney, K., et al. (2018). A community-developed open-source computational ecosystem for big neuro data. Nat. Methods *15*, 846–847.

Wang, Y., Kim, J., Schmit, M.B., Cho, T.S., Fang, C., and Cai, H. (2019). A bed nucleus of stria terminalis microcircuit regulating inflammation-associated modulation of feeding. Nat. Commun. *10*, 2769.

Wang, Q., Ding, S.-L., Li, Y., Royall, J., Feng, D., Lesnar, P., Graddis, N., Naeemi, M., Facer, B., Ho, A., et al. (2020). The allen mouse brain common coordinate framework: a 3D reference atlas. Cell *181*, 936–953.e20.

Wu, J., Silversmith, W.M., Lee, K., and Seung, H.S. (2019). Chunkflow: distributed hybrid cloud processing of large 3d images by convolutional nets. Front. Neural Circuits *13*, 1–9.

Xu, X., Roby, K.D., and Callaway, E.M. (2010). Immunochemical characterization of inhibitory mouse cortical neurons: three chemically distinct classes of inhibitory cells. J. Comp. Neurol. *518*, 389–404.

Yang, B., Treweek, J.B., Kulkarni, R.P., Deverman, B.E., Chen, C.K., Lubeck, E., Shah, S., Cai, L., and Gradinaru, V. (2014). Single-cell phenotyping within transparent intact tissue through whole-body clearing. Cell *158*, 945–958.

Yeo, S.-H., Kyle, V., Blouet, C., Jones, S., and Colledge, W.H. (2019). Mapping neuronal inputs to Kiss1 neurons in the arcuate nucleus of the mouse. PLoS One *14*, e0213927.

Yushkevich, P.A., Piven, J., Hazlett, H.C., Smith, R.G., Ho, S., Gee, J.C., and Gerig, G. (2006). User-guided 3D active contour segmentation of anatomical structures: significantly improved efficiency and reliability. NeuroImage *31*, 1116–1128.

Zhang, C., Yan, C., Ren, M., Li, A., Quan, T., Gong, H., and Yuan, J. (2017). A platform for stereological quantitative analysis of the brain-wide distribution of type-specific neurons. Sci. Rep. *7*, 14334.

STAR★METHODS

KEY RESOURCES TABLE

REAGENT or RESOURCE	SOURCE	IDENTIFIER
Antibodies		
Mouse anti-PV antibody Dilution 1:50	Swant	Cat# PV235
Rat anti-SST antibody Dilution 1:10	Millipore	Cat# MAB354, RRID AB_2255365
Rabbit anti-ChAT antibody Dilution 1:200	Abcam	Cat# ab178850, RRID AB_2721842
Mouse anti-Th antibody Dilution 1:20	Santa Cruz Biotechnology	Cat# sc-25269, RRID AB_628422
Rabbit anti-Iba1 antibody red fluorochrome(635)-conjugated Dilution 1:50	Wako	Cat# 013-26471, RRID AB_2687911
Mouse anti-6E10 antibody Dilution 1:75	BioLegend	Cat# 93049, RRID AB_2715854
Rabbit anti-c-Fos antibody Dilution 1:100	Cell Signaling Technology	Cat# 2250S, RRID AB_2247211
Goat anti-Mouse IgG1, Fcγ fragment specific, Cy3, Dilution 1:150	Jackson ImmunoResearch	Cat# 115-167-185 RRID AB_2632514
Goat anti-Rat IgG, Fcγ fragment specific, Alexa Fluor 594, Dilution 1:150	Jackson ImmunoResearch	Cat# 112-587-008, RRID AB_2632490
Goat anti-Rabbit IgG, Fcγ fragment specific, Alexa Fluor 594, Dilution 1:150	Jackson ImmunoResearch	Cat# 111-587-008 RRID AB_2632469
Goat anti-Mouse IgG2a, Fcγ fragment specific, Alexa Fluor 594, Dilution 1:150	Jackson ImmunoResearch	Cat# 115-587-186, RRID AB_2632540
Bacterial and virus strains		
AAV9-CAG-FLEx-TCb	Miyamichi et al., 2013 (Custom made by Penn Vector Core)	N/A
AAV9-CAG-FLEx-oG	Kim et al., 2016 (Custom made by Penn Vector Core)	N/A
Rabies ΔG-GFP+EnvA	Osakada and Callaway, 2013 (Amplified in the lab from a virus shared by Dr. Masahiro Yamaguchi)	N/A
Deposited data		
Whole-brain expression analysis of PV (analyzed data)	This study	https://cubic-cloud.com
Whole-brain expression analysis of PV (raw image)	This study	http://cubic-atlas.riken.jp/
Whole-brain expression analysis of SST (analyzed data)	This study	https://cubic-cloud.com
Whole-brain expression analysis of SST (raw image)	This study	http://cubic-atlas.riken.jp/
Whole-brain expression analysis of ChAT (analyzed data)	This study	https://cubic-cloud.com
Whole-brain expression analysis of ChAT (raw image)	This study	http://cubic-atlas.riken.jp/
Whole-brain expression analysis of TH (analyzed data)	This study	https://cubic-cloud.com
Whole-brain expression analysis of TH (raw image)	This study	http://cubic-atlas.riken.jp/

(*Continued on next page*)

Continued

REAGENT or RESOURCE	SOURCE	IDENTIFIER
Whole-brain expression analysis of Iba1 (analyzed data)	This study	https://cubic-cloud.com
Whole-brain expression analysis of Iba1 (raw image)	This study	http://cubic-atlas.riken.jp/
Whole-brain antibody staining Ab plaque (6E10) (analyzed data)	This study	https://cubic-cloud.com
Whole-brain antibody staining Ab plaque (6E10) (raw image)	This study	http://cubic-atlas.riken.jp/
Whole-brain expression analysis of c-Fos (LPS and control condition) (analyzed data)	This study	https://cubic-cloud.com
Whole-brain expression analysis of c-Fos (LPS and control condition) (raw image)	This study	http://cubic-atlas.riken.jp/
Whole-brain circuit analysis of ARH^{Kiss1} using Rabies virus (analyzed data)	This study	https://cubic-cloud.com
Whole-brain circuit analysis of ARH^{Kiss1} using Rabies virus (raw image)	This study	http://cubic-atlas.riken.jp/
Experimental models: organisms/strains		
Mouse strain *App*$^{NL-G-F/NL-G-F}$	RIKEN BioResource Research Center	RBRC No. RBRC06344, RRID IMSR_RBRC06344
Mouse strain *Kiss1*$^{tm1.1(cre/EGFP)Stei}$/J	Jackson Laboratory	Stock No. 017701, RRID IMSR_JAX:017701
Software and algorithms		
Fiji	NIH	RRID SCR_02285
Python Anaconda distribution	Anaconda	https://www.anaconda.com RRID SCR_018317
ITK-SNAP	Yushkevich et al., 2006	RRID SCR_002010
ANTS	Avants et al., 2008	RRID SCR_004757
Ecc	This study	https://github.com/DSPsleeporg/ecc
CUBIC-Cloud	This study	https://cubic-cloud.com

RESOURCE AVAILABILITY

Lead contact

Further information and requests for resources and reagents should be directed to and will be fulfilled by the lead contact, Hiroki R. Ueda (uedah-tky@umin.ac.jp).

Materials availability

This study did not generate new unique reagents.

Data and code availability

Raw 3D image data analyzed in this study are available at http://cubic-atlas.riken.jp through an interactive image viewer powered by CATMAID (Saalfeld et al., 2009). The analyzed whole-brain data in point cloud format is deposited on http://cubic-atlas.riken.jp, as well as CUBIC-Cloud's public repository. The additional data that support the findings of this study are available from the corresponding author upon reasonable request.

Cell detection program used in this study is available at GitHub code repository (https://github.com/DSPsleeporg/ecc). CUBIC-Cloud computing service is accessible at https://cubic-cloud.com.

CUBIC-Cloud offers both free and paid subscription plans. CUBIC-Cloud is free for use for viewing data. Free plan users can also try analysis of several brains using the tokens supplied at the initial sign-up. Requests to upload brains or create notebooks over the free use limit are handled for a fee, to cover and compensate the maintenance cost of the cloud server.

EXPERIMENTAL MODEL AND SUBJECT DETAILS

Mice

All experimental procedures and housing conditions were approved by the Animal Care and Use Committee of The University of Tokyo. *App*$^{NL-G-F/NL-G-F}$ mice were provided by RIKEN BioResource Research Center (RBRC No. RBRC06344) (Saito et al., 2014). Kiss1-Cre mouse was purchased from The Jackson Laboratory (Kiss1-tm1.1(cre/EGFP)Stei/J, stock no. 017701). In all experiments, male mice were used unless otherwise specified. 8- to 14-weeks-old animals were used for experiments (for details see the STAR Method section of each experiment).

To sample brains, animals were anesthetized by an overdose of pentobarbital (> 100 mg/kg), then transcardially perfused with 10 mL of PBS (pH 7.4) and 20 mL of 4% paraformaldehyde (PFA). The brains were dissected, post-fixed in 4% PFA overnight at 4°C and stored in PBS.

METHOD DETAILS

Tissue clearing and whole-brain 3D immunostaining

To clear brain tissues, we used second-generation CUBIC protocols (Tainaka et al., 2018; Matsumoto et al., 2019). For delipidation, we used CUBIC-L (10 wt% *N*-butyldiethanolamine, 10 wt% Triton X-100), and for RI matching, either CUBIC-R+(N) (45 wt% Antipyrine, 30 wt% Nicotinamide, 0.5 vol% *N*-butyldiethanolamine) or CUBIC-R+(M) (45 wt% Antipyrine, 30 wt% *N*-methylnicotinamide, 0.5 vol% *N*-butyldiethanolamine) was used. CUBIC-R+(M) was used for samples labelled by fluorescent proteins (FPs) because of its better FP signal retention, and CUBIC-R+(N) was used otherwise. For all brains, nuclear staining (using either SYTOX-G, BOBO-1 or RedDo2) was applied. For whole-mount 3D immunostaining, we followed CUBIC-HV protocol (Susaki et al., 2020)). The details on antibody staining for each experiment can be found in the corresponding sections in STAR Method. Before imaging, the sample was embedded in a transparent agarose gel so that it could be rigidly mounted on a microscope stage (Murakami et al., 2018; Matsumoto et al., 2019).

LSFM imaging

A custom-built macro-zoom LSFM (named GEMINI system) was used to image cleared brains (the details of this microscope can also be found in (Susaki et al., 2020)). For illumination, the microscope was equipped with 488, 532, 594 and 642 nm diode or DPSS lasers (SOLE-6, Omicron). The laser sheet was generated by a cylindrical lens and the sheet thickness was adjustable by a mechanical slit. For detection, the microscope was equipped with 0.63X macro-zoom objective lens (MVPLAPO 0.63X, Olympus) and 0.63-6.3X variable zoom optics (MVX-ZB10, Olympus). After passing a suitable fluorescence filter, the fluorescence signal was captured by sCMOS camera (Zyla 5.5, Andor).

To achieve homogeneous light-sheet thickness throughout the field of view, several rectangular image strips with shifted illumination focus were obtained and digitally stitched together, similar to the approach used in TLS-SPIM (Gao, 2015; Fu et al., 2016). The width of the rectangular strip was matched with the Rayleigh range of the illumination light-sheet. In our setup, the sheet thickness was approximately 10 μm and the rectangular strip width was 1500 μm, which required 6 image strips to cover the entire brain.

For RV samples, the image voxel size was (X,Y,Z) = (8.25, 8.25, 9.0) μm with 1.2X intermediate zoom optics. For other experiments, the voxel size was (X,Y,Z) = (6.45, 6.45, 7.0) μm with 1.6X intermediate zoom optics. It should be noted that the effective resolution should take into account the moderate tissue expansion (∼1.5X) caused by CUBIC-R treatment.

For each dye/FP, the following laser and fluorescence filter pair was used: Alexa 594 [Ex: 594 nm, Em: 641/75 nm bandpass (FF02-641/75-32, Semrock)], Cy3 [Ex: 532 nm, Em: 585/40 nm bandpass (FF01-585/40-32, Semrock)], SYTOX-G, BOBO-1 and GFP [Ex: 488 nm, Em: 520/40 nm bandpass (FF01-520/44-32, Semrock)], RedDot2 [Ex: 642nm, Em: 708/75 nm bandpass (FF01-708/75-32, Semrock)], mCherry [Ex: 594 nm, Em: 628/32 nm bandpass (FF01-628/32-32, Semrock)].

Imaging the fluorescent bead embedded in cleared tissue

1.0 μm-diameter green-yellow fluorescent beads (Thermo Fisher, #F8765) were diluted in PBS so that the final bead concentration was 0.9×10^7 particles/ml. This bead-mixed PBS solution was perfused in mice, prior to the PFA perfusion. Because the bead surface was modified with amine, PFA was able to cross-link and fix the beads within the tissue. After tissue clearing, the whole brain was imaged using the macro-zoom LSFM with XYZ voxel resolution of 6.45x6.45x7.0 μm (Figure S2A). Then, single and well-isolated bead particles were manually annotated (n>15 for each brain region) using ITK-SNAP software (Yushkevich et al., 2006). Subsequently, the mean spot profiles were computed and fitted with Gaussian using custom Python code. The fitted sigma values from six regions were all within 4.4 to 4.9 μm (lateral) and 5.3 to 6.7 μm (axial) (Figure S2B), validating homogeneous image quality throughout the entire brain. Given the digital sampling frequency (6.5 μm) of the microscope used, this result was nearly the ideal PSF.

Using the same data, we have also quantified the absolute bread fluorescent intensity of different brain areas (Figure S2C). The graph indicates that the thalamus, which is most distant from the brain surface, showed relatively lower brightness, reflecting the attenuation of the illumination beam as well as the emitted fluorescence by the tissue. Nonetheless, the differences in magnitude between regions were less than two-fold, which we concluded is good enough for quantitative analysis.

Cell detection

The cell detection workflow used in this study is shown in Figure 1A (”step 3”). As the first step, a machine-learning algorithm was used to classify voxels into labelled cells and other structures. For this step, we used ilastik (Sommer et al., 2011). To train the classifier, for each label type (such as c-Fos), manual annotation images were prepared. In this study, three classes were defined, which were (1) signals of interest, i.e., cells labelled by FPs or antibodies (2) bright but false signals, such as non-specific binding of antibodies to vascular structures or neurites extending from cell bodies and (3) background (i.e. void space). Typically, 5,000 to 10,000 voxels were annotated as class 1 per one dataset. To increase the robustness, at least two brains with identical labelling conditions were annotated. Image annotation was performed using ITK-SNAP software (Yushkevich et al., 2006).

Next, following the ilastik workflow, image feature descriptors were selected to distinguish the three classes defined above. For PV, Sst, ChAT, Th, Iba1, c-Fos, RV-GFP and AAV-mCherry images, the selected descriptors were Gaussian (= 0.3, 0.7 voxel), Gaussian gradient magnitude (= 0.7 voxel), difference of Gaussian (= 0.7, 1.0, 1.6, 3.5 voxel) and Hessian of Gaussian eigenvalues (= 1.0, 1.6, 3.5 voxel). For A images, difference of Gaussian (= 5.0 voxel) and Hessian of Gaussian eigenvalues (= 5.0 voxel) were additionally included, so that the larger spatial context was taken into account. Then, ilastik software trained the voxel classifier using random forest algorithm. Hyperparameters related to random forest algorithm was automatically configured by ilastik. After the classifier was trained, it was applied to the test dataset to evaluate accuracy. If obvious error was present, manual annotation data were further supplemented, so that the classifier became more robust against such errors. Once the classifier achieves satisfactory accuracy, it could reliably be applied to other images with the same label type.

By applying the voxel classifier trained above to each brain image, a probability image was produced, where the value of each voxel represents the probability of that voxel being class 1 (Figure S3A). The probability value was given in the range [0, 1]. Using this probability image, a custom Python program isolated individual cells in the following way. First, the probability threshold, $P_{th} = 0.7$, was applied to make a binarized image. Then, connected voxels were searched and merged together, to find individual objects. If the identified object volume was larger than a threshold, V_{th}, it was sent to the object separation routine. The object separation routine simply finds local maxima with an exclusion distance $r_{excl} = V_{th}^{1/3}$. V_{th} was heuristically determined to be $V_{th} = 4^3 = 64$ for PV, Sst, c-Fos, Iba1, Rabeis-GFP and AAV-mCherry, and $V_{th} = 5^3 = 125$ for ChAT and Th. For A plaque segmentation, $V_{th} = \infty$ was used. Hence, there are two free parameters (P_{th} and V_{th}), both of which can be intuitively determined.

Using 20 CPU cores, cell detection of one 3D image stack (typically 2560x2160x1200 voxels) took about 1 h to complete.

The Python source code and its documentation is available at https://github.com/DSPsleeporg/ecc.

Accuracy evaluation of cell detection

Accuracy of the above explained cell detection procedure was extensively evaluated by comparing automated counting results with manual cell counting (Figure S3B-H). Manual cell counting was performed by cropping a small cubic image volume (50 or 75 or 100 voxels, depending on the cell density) from brain images which were not used in machine learning training. Well-trained human annotators ($n = 2$) independently marked all of the cells present in the image and typically yielded 100-200 marked cells. Image annotation was performed using ITK-SNAP software (Yushkevich et al., 2006). Cells annotated by both human and algorithm were regarded as true positives. Cells annotated by human but not by algorithm was regarded as false negative. Cells annotated by algorithm but not by human were regarded as false positives. Then, true positive rate (TPR, also called sensitivity) and positive predictive value (PPV, also called precision) were evaluated for each human annotator. To quantify the overall performance, F1 score, defined as $F1 = 2 * (PPV \times TPR)/(PPV + TPR)$, was also evaluated. For most of the label types and brain regions, our cell detection algorithm robustly demonstrated good F1 scores, with average score being 0.80 (PV), 0.83 (Sst), 0.88 (ChAT), 0.80 (Th), 0.88 (Iba1), 0.83 (c-Fos) and 0.89 (GFP).

Raw 3D image data, along with markers highlighting all detected cells, are available at http://cubic-atlas.riken.jp through an interactive image viewer powered by CATMAID (Saalfeld et al., 2009).

CUBIC-Atlas

CUBIC-Cloud uses CUBIC-Atlas version 1.1 (Murakami et al., 2018) as the reference brain coordinate, to which all individual brain data were mapped. From the originally published atlas (version 1.0), we added a few minor updates in this study to generate CUBIC-Atlas version 1.1. The updates included (1) slight discontinuity between dorsal and ventral image volume (so-called ”theta tile displacement” in Murakami et al. paper) were corrected and (2) region annotation was updated to be compatible with the Allen Brain Atlas CCFv3 (October 2017). CUBIC-Atlas v1.1 can be downloaded from http://cubic-atlas.riken.jp.

Brain registration

CUBIC-Cloud uses the symmetric image normalization (SyN) algorithm implemented in ANTs library (Avants et al., 2008) to run registration between CUBIC-Atlas (”fixed” brain) and individual brain sample (”moving” brain). First, nuclear staining image of the ”moving” image was downscaled to a voxel size of 50x50x50 μm. Nuclear staining image of CUBIC-Atlas was downscaled to a voxel size of 80x80x80 μm. Considering the sample’s physical expansion by clearing treatment (2.2X for CUBIC-Atlas and 1.5X for CUBIC-R+ treated brains), this downscaling operation resulted in an effective voxel size of about 35x35x35 μm in both images. The registration first computed affine transformation to coarsely align the orientation and size, using mutual information as the optimizer metric. Subsequently, non-linear warping was computed by SyN algorithm, which optimized the warp field by maximizing the normalized

cross-correlation (NCC) between the two images under diffeomorphic regularization (Avants et al., 2008). Given image $I(\mathbf{x})$ and image $J(\mathbf{x})$, the NCC value between I and J at the voxel position $\mathbf{x}$ is given by

$$NCC(I,J,\mathbf{x}) = \frac{\langle \bar{I}, \bar{J} \rangle}{|\bar{I}||\bar{J}|} \quad \text{(Equation 1)}$$

where $\langle A, B \rangle$ represents the inner product taken over a local window with radius R centered at position $\mathbf{x}$. $|A|$ is the L2 norm of the vector computed over a local window with radius R. Here, $\bar{I}(\mathbf{x}) = I(\mathbf{x}) - \mu_I(\mathbf{x})$ means the subtraction of the local mean, where local mean $\mu_I(\mathbf{x})$ is computed over a local window with radius R centered at position $\mathbf{x}$. $R = 4$ (voxels) was used throughout our brain registration.

Other detailed parameters used in the ANTs registration are the following. In the first affine transformation stage, the pseudo ANTs command below was used.

```
—transform Affine[0.1] \
—metric MI[X,Y,1,128,Regular,0.5] \
—convergence [1000x1000x1000,1e-5,15] \
—shrink-factors 8x4x2 \
—smoothing-sigmas 3x2x1vox
```

In the second SyN transformation stage, the pseudo ANTs command below was used.

```
—transform SyN[0.1,3.0,0.0] \
—metric CC[X,Y,1,4] \
—convergence [500x500x500x50,1e-6,10] \
—shrink-factors 8x4x2x1 \
—smoothing-sigmas 3x2x1x0vox
```

In addition, `-winsorize-image-intensities [0.05,1.0]` and `-use-histogram-matching 0` was used throughout.

The representative registration result is visualized in Figure S3I, along with the NCC value heatmap (Figure S3L). To show the reproducibility of the registration, 20 individual brains were mapped onto CUBIC-Atlas with identical registration parameters. The mean NCC value of each coronal planes were computed and plotted (Figure S3H). 20 independent curves overlap with each other, meaning that the optimization attempt by the registration reached saturation. NCC value tends to show higher value in the olfactory area and cerebellum, due to the presence of more distinct structural features.

CUBIC-Cloud users can check and validate the registration accuracy of their own brain by looking at the NCC value map and the summarized plot, which can be downloaded from the ''Downloads'' list of the brain detail window.

Registration between CUBIC- and iDISCO-cleared brains

C57BL/6N mouse brain (male, 8-weeks-old, $n = 2$) were cleared by iDISCO method following the standard protocol (Renier et al., 2014, 2016). The cell nuclei staining was performed by incubating the sample with 2 uM TO-PRO-3 (ThemoFisher #T3605) dissolved in PTwH solution for 5 days at 37°C. The cleared brain was scanned with LSFM with (X,Y,Z) = (6.5, 6.5, 7.0) μm resolution.

Prior to running registration, the nuclear staining image was downscaled to (X,Y,Z) = (30, 30, 30) μm voxel resolution. Using ANTs, registration with CUBIC-Atlas was performed using the same parameters as described above. The representative registration result is shown in Figure S4A. A series of coronal slice images are shown in Figure S4C, along with the corresponding normalized cross-correlation (NCC) values represented as a heatmap (Figure S4D). The mean of NCC in each coronal slice was plotted in Figure S4B. As is shown in this plot, the iDISCO-brain registration resulted in similar NCC values as CUBIC-brain registration in most of the brain areas, indicating that the registration method was able to align the iDISCO-cleared brain with the comparable accuracy. However, the registration accuracy was poor in the olfactory bulb (Figures S4A–S4C). Indeed, the morphology of olfactory bulb is affected in the CUBIC clearing process, where the organ is expanded and a gap between left and right bulb is widened. Although we have attempted to tune the registration parameters to overcome this misalignment, no parameters we tested was able to give accurate alignment in the olfactory bulb. SyN transformation method implemented in ANTs penalizes the deformation where neighboring deformation vectors are not aligned. This strongly penalizes the deformation where the gap between olfactory bulb is widened or shrunk, because the deformation vector flips the orientation at the center. We presume that this is the reason why the registration in the olfactory bulb was not successful, and further research would be needed to overcome this challenge.

Architecture of CUBIC-Cloud

CUBIC-Cloud's entire application stack is deployed on the cloud computing infrastructures offered by Amazon Web Service (AWS). The cloud is constructed using the serverless architecture (Adzic and Chatley, 2017). Serverless architecture have zero real instances that are always running; instead, the cloud is composed by connecting microservices, which are dynamically invoked by events. Such cloud design eliminates the cost of idling servers, while allowing to flexibly and instantly scale out the computing power when the traffic or load to the service increases.

The schematic illustration of the cloud architecture is shown in Figure S1. When user accesses the web site, the trafic is first handled by CloudFront. CloudFront is responsible for caching static contents, managing SSL/TLS and web application firewall (WAF). Then, static web contents are fetched from S3 bucket and returned to the user. User authentication is handled by Cognito. Once authenticated, users can access the protected API endpoints securely using json web token (JWT). All REST API requests are routed by API Gateway and handled by Lambda. Lambda handlers have access to various back-end resources, including the databases and the data buckets. The metadata of the users, brains, notebooks, and studios are stored in DynamoDB. Large data files (such as images and csv tables) are stored in S3.

Once a user uploads the brain data, the upload completion event from S3 triggers a ''preprocessing'' task in the Elastic Container Service (ECS) cluster. Preprocessing includes brain registration, transformation, and data conversion. ECS automatically launches a new Elastic Compute Cloud (EC2) instance, pulls the Docker container from Elastic Container Registry (ECR), and initiate a new task. The task execution is orchestrated by StepFunctions. Notebook tasks (i.e. generating plots) are similarly orchestrated by StepFunctions, except that the runtime is either Lambda or Fargate, depending on the required memory size of the task.

Most of the API handlers are written in Python. The cloud resources are managed by AWS CDK library for Python, and the cloud is deployed using the CloudFormation generated by the CDK library. The user interfaces (UIs) were constructed using HTML/CSS/JavaScript and Vue.js framework.

A web-based whole-brain viewer

CUBIC-Cloud offers a point-cloud based interactive 3D brain viewer, a feature called studio. The viewer is written in JavaScript, and runs in most of the standard web browsers, including Google Chrome and Firefox. It uses WebGL for hardware accelerated 3D rendering. The core of the point cloud rendering engine was adopted from the open-source project, Potree (2016). Following Potree, CloudEye uses a specialized point cloud format where the whole point cloud was divided and stored in a multi-resolution hierarchical structure (octree structure). This hierarchical data structure enabled the adaptive data querying in response to client's viewpoint, in which a portion of the points near the viewer's camera was selectively loaded. The octree-formatted point cloud data were automatically generated as a part of the preprocessing task in the CUBIC-Cloud server. Each point can be attached with several attributes, including the region ID and fluorescent intensity. Points may be colored using these attributes. For example, points may be given gradient colors based on their fluorescence intensity values.

Users can navigate and explore the whole-brain data by intuitive mouse interactions. Points can be selectively hidden/displayed based on the region ID. Arbitrary combinations of brains may be overlaid with user-defined colors. Users can also make a slice view, which can be moved or rotated with simple mouse dragging. Users can also grab a point (cell) and query its information, such as fluorescent intensity.

Privacy and data ownership policy of CUBIC-Cloud

CUBIC-Cloud has rigorously defined the privacy and data ownership policy, which can be viewed at the CUBIC-Cloud's web site (https://cubic-cloud.com/terms and https://cubic-cloud.com/privacy). In essence, all data stored in the user's private space solely belongs to the user and all intellectual properties are protected. When a user decides to publish in the public repository, the depositor shall grant unrestricted use of the data to all other users in CUBIC-Cloud.

Whole-brain analysis of PV and SST expressing neurons

C57BL/6N wild-type mice brains (8-week-old, $n = 4$) were cleared, stained, imaged, and analyzed as described in the corresponding sections in STAR Method. Brains were stained with PV antibody (Swant, #PV235; 1/50 dilution; anti-mouse IgG1 secondary Fab fragment conjugated with Cy3 (Jackson ImmunoResearch, #115-167-185)), SST antibody (Millipore, #MAB354; 1/10 dilution; anti-rat IgG secondary Fab fragment conjugated with Alexa 594 (Jackson ImmunoResearch, #112-587-008)) and nuclear staining dye (BOBO-1, Thermo Fisher #B3582). The whole-brain summary of detected PV+ and SST+ cells are provided in Table S1.

We discussed the PV+ and SST+ cell in the isocortex in the main text. Within the striatum, PV+ cells were almost entirely absent in the LS and anterior, central, intercalated and medial amygdalar nucleus (AAA, CEA, IA and MEA), as observed previously (McDonald and Betette, 2001). Distribution in the brain stem faithfully reproduced the previous slice-based immunohistochemical studies (Celio, 1990; Johansson et al., 1984) (Figure 2L). In general, the thalamus contained low numbers of PV+ or SST+ cells, except that dense PV+ cells were present in the RT and PP. In the hypothalamus, although PV+ cells were sparse, many nuclei contained medium to high density of SST+ neurons. Within the midbrain, PV+ cells were particularly abundant in the IC and SNr, while SST+ cells were most frequently observed in the RAmb. Within the pons and medulla, the NTB, SOC and NLL contained both PV+ and SST+ cells with relatively high density, while sparsely scattered populations were observed in other areas. In the cerebellum, there were a large number of PV+ neurons in Purkinje layers. Distinct SST+ cell clusters were found in the NOD and FL.

Whole-brain analysis of ChAT expressing neurons

C57BL/6N wild-type mice brains (8-week-old, $n = 4$) were cleared, stained, imaged and analyzed as described in the corresponding sections in STAR Method. Brains were stained with ChAT antibody (abcam, #ab178850; 1/200 dilution; anti-rabbit IgG secondary

Fab fragment conjugated with Alexa 594 (Jackson ImmunoResearch, #111-587-008)) and nuclear staining (SYTOX-G, Thermo Fisher, #S7020). The whole-brain summary of detected ChAT+ cells are provided in Table S1.

About half of ChAT+ cells were concentrated in striatum and pallidum (34.5% and 13.8%, respectively). Continuously spreading from these regions, some ChAT+ cells were present in the hypothalamus, including lateral, medial and anteroventral preoptic areas (LPO, MPO, AVP) and SO. ChAT+ neurons were hardly observed in the olfactory area, hippocampus, cortical subplate and thalamus. These observations were in good agreement with the slice-based immunohistochemical study by Armstrong et al., 1983.

Whole-brain analysis of Th expressing neurons

C57BL/6N wild-type mice brains (8-week-old, $n = 4$) were cleared, stained, imaged and analyzed as described in the corresponding sections in STAR Method. Brains were stained with Th antibody (Santa Cruz Biotechnology, #sc-25269; 1/20 dilution; anti-mouse IgG2a secondary Fab fragment conjugated with Alexa 594 (Jackson ImmunoResearch, #115-587-186)) and nuclear staining (SYTOX-G). The whole-brain summary of detected Th+ cells are provided in Table S1.

The majority of the detected Th neurons were localized in well-known dopaminergic cell groups (A8 to A16) and noradrenergic cell groups (A1 to A7) (Dahlström and Fuxe, 1964). Dopaminergic cell groups include the RR, SNc, rostral and central linear nucleus raphe (RL and CLI) and VTA, which form the A8, A9 and A10 in midbrain. Within the hypothalamus, Th neurons were clustered in the periventricular hypothalamic nucleus, anterior, posterior, intermediate and propotic parts (PVa, PVp, PVi, PVpo), ARH, ZI and ADP, which form A11-A15 cell groups. Th neurons were numerous in the olfactory area (A16), selectively localized in the glomerular layer. Noradrenergic cell groups formed distinct bands crossing several nuclei in the medulla and pons, which included the LRN, NTS and DMX, which form A1 and A2. In the pons, a particularly high density was observed in and around LC, which forms A6. No significant population of Th+ cells were observed in the isocortex, hippocampus, cortical subplate, striatum and pallidum.

Brain nuclei segmentation using alpha shape algorithm

A densely aggregated ChAT expressing cells were found in the LDT and its neighboring regions. To segment this brain region automatically, a rectangular region containing these cells were manually cropped. Then, to remove the isolated cells that was not part of the continuous body of the nuclei, the following filter was applied: for each cell in the ensemble, the number of neighboring cells within the radius 100 μm were counted, and if the count is less than 2, the cell was removed from the ensemble. After this filtering, the polygonal surface enclosing the points was constructed using alpha shape algorithm with alpha radius parameter 300 μm, implemented in MATLAB. This method was applied to $n = 4$ brains aligned with CUBIC-Atlas, obtaining four independent boundary surfaces. Using the same method, cluster of TH expressing cells around LC were segmented ($n = 4$).

Lastly, the overlap between ChAT-defined boundaries were evaluated by computing the Dice's coefficient, $c = (2 * V_{V1 \cap V_2}) / (V_1 + V_2)$ where $V_{V1 \cap V_2}$ is the volume of the overlap between the two polygons whose volumes are V_1 and V_2, respectively. The Dice's coefficient of all possible pairs, $\binom{4}{2} = 6$, were evaluated. The same analysis was applied to TH-defined boundaries. Lastly, the overlaps between ChAT and TH boundaries were evaluated by picking all possible pairs, $4^2 = 16$.

Whole-brain analysis of Iba1 expressing cells

C57BL/6N wild-type mice (8-week-old, $n = 7$ for LPS-administered and control group, respectively) were administered with either 1 mg/kg of LPS or saline via i.p. injection. 24 h after injection, brains were sampled. Subsequently, brains were cleared, stained, imaged and analyzed as described in the corresponding sections in STAR Method. Brains were stained with Iba1 antibody (Wako, #013-26471; 1/50 dilution; directly conjugated with red dye) and nuclear staining (SYTOX-G). The whole-brain summary of detected Iba1+ cells are provided in Table S2.

Whole-brain analysis of Aβ plaques

*App*NL-G-F/NL-G-F mice (9- to 10-month-old, $n = 4$) were cleared, stained, imaged and analyzed as described in the corresponding sections in STAR Method. Brains were stained with -Amyloid (6E10) antibody (Biolegend, #93049; 1/100 dilution; anti-mouse IgG1 secondary Fab fragment conjugated with Alexa 594 (Jackson ImmunoResearch, #115-587-185)) and nuclear staining (SYTOX-G).

Whole-brain analysis of c-Fos profile change induced by LPS

To monitor the sleep duration of mice in an non-invasive manner, we used a respiration-based sleep staging method, SSS (Sunagawa et al., 2016). C57BL/6N wild-type mice (8-week-old, $n = 4$ each for LPS-administered and control group) were housed in a SSS chamber for 3 days (basal measurement; LD cycle) prior to the injection. On the fouth day at ZT = 14, mice were administered 150 μg/kg LPS from Escherichia coli (Sigma-Aldrich, #L2990) via i.p. injection, while control mice were administered saline (Figure S7D). After injection, mice were housed in the SSS chamber for another 24 h to monitor sleep.

Brains for whole-brain imaging were collected in a replicate experiment with the identical conditions as above, except that mice were housed in DD cycle and that brains were sampled at CT = 16-17 after i.p. injection ($n = 4$ in total for each group, obtained in 1 batch). Collected samples were cleared, stained, imaged and analyzed as described in corresponding sections in STAR Method.

Brains were stained by c-Fos antibody (CST, #2250S; 1/75 dilution; anti-rabbit IgG secondary Fab fragment conjugated with Alexa 594 (Jackson ImmunoResearch, #111-587-008)) and nuclear staining dye (SYTOX-G).

Rabies virus injection

The following AAV vectors were generated de novo by PENN vector core using the corresponding plasmids. AAV serotype 9 CAG-FLEx-TCb (1.5×10^{13} gp/ml) was made using the plasmid described previously (Miyamichi et al., 2013). Here TCb stands for TVA-mCherry expression cassette optimized to increase mCherry brightness. To generate AAV serotype 9 CAG-FLEx-oG (4.5×10^{13} gp/ml), engineered and optimized glycoprotein (oG) (Kim et al., 2016) sequence was ligated to pAAV-FLEX sequence from pAAV-FLEX-GFP (Addgene).

Preparation of rabies virus was conducted by using the RVG-GFP, B7GG and BHK-EnvA cells as previously described (Osakada and Callaway, 2013). The EnvA-pseudotyped RVG-GFP+EnvA titer was estimated to be 1.0×10^{9} infectious particles/ml based on serial dilutions of the virus stock followed by infection of the HEK293-TVA800 cell line (a gift from Dr. Edward Callaway at Salk Institute).

For trans-synaptic tracing using rabies virus, about 20 nL of mixture of AAV9 CAG-FLEx-TCb and CAG-FLEx-oG (diluted to 1.5×10^{12} gp/ml each) was injected into the ARH of Kiss1-Cre mice. The first AAV transduced a TVA receptor (fused with mCherry) for EnvA. The second AAV transduced RV glycoprotein (oG) playing a predominant role in the trans-synaptic transport of RV. The injection coordinate was P1.1, L0.2, V5.9 (distance in mm from the Bregma for the posterior [P], and lateral left [L] positions and from the brain surface for the ventral [V] position). Three weeks later, 30 nL of Rabies G-GFP+EnvA was injected into the same brain region to initiate trans-synaptic tracing. Because there is no cognate receptor for EnvA in the mouse brain, RVG+EnvA only infects TVA-expressing cells. oG expression from the second AAV complements the RVG, allowing retrograde monosynaptic tracing from Cre-expressing cells. Seven days later, brains were sampled for CUBIC treatment.

Whole-brain analysis of RV-injected brains

After AAV and RV injection, Kiss1-Cre mice (13- or 14-week-old at the time of brain sampling) were cleared, stained, imaged and analyzed as described in the corresponding sections in STAR method. Brains were stained with nuclear staining (RedDot2, Biotium, #40061).

As a negative control experiment, AAV and RV injection was performed using BALB/c wild-type mice brain ($n = 3$). After clearing, the whole-brain image was obtained by LSFM. No GFP or mCherry signals were observed by manual inspection, confirming the absence of Cre-indepentent leakage of AAV vectors and specificity of the virus delivery.

Starter cells were searched by identifying dual positive (mCherry+ and GFP+) cells. For each channel, cell counting was independently performed, and the center of the mass of the detected cell was obtained. For each mCherry+ cells, if a GFP+ cell was present within a distance of 24 μm, the cell was counted as starter. Note that because the cleared tissue was expanded by a factor of ~ 1.5, this was roughly 16 μm in untreated tissue. Occasionally, slight voxel shift (typically no more than 4 voxels) occurred between GFP and mCherry channels, which was presumably caused by slight misalignment between the 488 nm and 594 nm illumination laser or re-focusing of the microscope. To correct this, small 3D volumes with distinct features (typically (X,Y,Z) = (50,50,20) voxel volume, $n =$ 4 or $n = 3$) from mCherry and GFP channels were cropped, and the voxel shift was computed by registering two images using ANTs, where transformation was restricted to only translation. Then, the cell coordinates were corrected by the mean of the computed shift.

To carry out statistical analysis of input cell numbers between male and female brains, we used the normalized cell count, $n_{\mathrm{norm},i}$, where i represents the ID of the brain region. If we let the raw cell number of each brain region be $n_{\mathrm{raw},i}$, $n_{\mathrm{norm},i}$ is simply expressed as $n_{\mathrm{norm},i} = n_{\mathrm{raw},i} / \left(\sum_i n_{\mathrm{raw},i} \right)$.

QUANTIFICATION AND STATISTICAL ANALYSIS

Statistical analysis

Statistical analysis used in each data are described in detail in the corresponding sections in the main text, supplementary materials or the figure legends. n (the number of samples) and *p-value*s are indicated in the corresponding sections in the main text, supplementary materials or the figure legends.